

QUADIM: A CONDITIONAL DIFFUSION MODEL FOR QUANTUM STATE PROPERTY ESTIMATION

Anonymous authors

Paper under double-blind review

ABSTRACT

Quantum state property estimation (QPE) is a fundamental challenge in quantum many-body problems in physics and chemistry, involving the prediction of characteristics such as correlation and entanglement entropy through statistical analysis of quantum measurement data. Recent advances in deep learning have provided powerful solutions, predominantly using auto-regressive models. These models generally assume an intrinsic ordering among qubits, aiming to approximate the classical probability distribution through sequential training. However, unlike natural language, the entanglement structure of qubits lacks an inherent ordering, hurting the motivation of such models. In this paper, we introduce a novel, non-autoregressive generative model called **QuaDiM**, designed for **Quantum** state property estimation using **Diffusion Models**. QuaDiM progressively denoises Gaussian noise into the distribution corresponding to the quantum state, encouraging equal, unbiased treatment of all qubits. QuaDiM learns to map physical variables to properties of the ground state of the parameterized Hamiltonian during offline training. Afterwards one can sample from the learned distribution conditioned on previously unseen physical variables to collect measurement records and employ post-processing to predict properties of unknown quantum states. We evaluate QuaDiM on large-scale QPE tasks using classically simulated data on the 1D anti-ferromagnetic Heisenberg model with the system size up to 100 qubits. Numerical results demonstrate that QuaDiM outperforms baseline models, particularly auto-regressive approaches, under conditions of limited measurement data during training and reduced sample complexity during inference.

1 INTRODUCTION

Quantum state property estimation (QPE) is a pivotal and challenging problem in the field of quantum many-body physics (Carleo & Troyer, 2017; Torlai et al., 2018; Carrasquilla, 2020; Gebhart et al., 2023; Miles et al., 2023) and chemistry (Kandala et al., 2017; Schütt et al., 2019; Cao et al., 2019; Sajjan et al., 2022; Barrett et al., 2022). The primary goal is to accurately infer certain properties of the quantum state such as correlation and entanglement entropy using as few quantum measurements as possible. QPE has wide-ranging applications in quantum computing (Dunjko & Briegel, 2018; Torlai & Melko, 2020), quantum cryptography (Brakerski & Shmueli, 2019; Ananth et al., 2022), and quantum simulation (Jia et al., 2019; Schmitt & Heyl, 2020). As the number of qubits in a system grows, the dimensionality of the corresponding quantum state increases exponentially, making property estimation increasingly difficult. Traditional techniques, like quantum state tomography (D’Ariano et al., 2003; Jullien et al., 2014), become impractical for large systems due to their exponential computational overheads.

Recent advancements in machine learning have opened new avenues for QPE, leveraging the models to extract intricate features from quantum measurement records. An overview about the pipeline is provided in Fig. 1. A notable way relies on auto-regressive models, which assumes an inherent order among qubits (e.g. left-to-right for 1D chain, or ZigZag order for 2D lattice) and decompose their joint probability distribution into conditional probabilities. These approaches include RNN-based models (Carrasquilla et al., 2019; Hibat-Allah et al., 2020; Barrett et al., 2022), CNN-based models (Wu et al., 2019; Sharir et al., 2020) and transformer-based models (Cha et al., 2021; Wang et al., 2022; Du et al., 2023; Tang et al., 2024). By learning from the records from quantum measurements, the trained model’s output would approximate the (classical) distribution of quantum

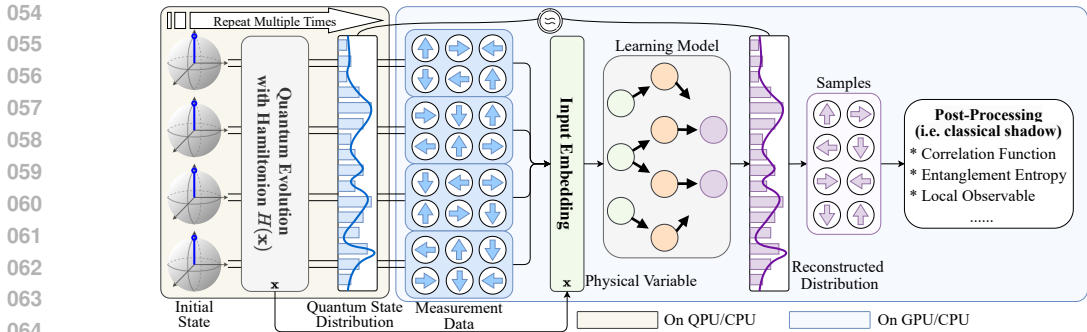


Figure 1: **An Overview of Quantum State Property Estimation.** Given the specified Hamiltonian $H(\mathbf{x})$ parameterized by \mathbf{x} , the quantum system initiates from state $|\psi_s\rangle$ and evolves controlled by $H(\mathbf{x})$ in either physical experiments on a quantum processing unit (QPU) or simulations on CPUs. Measurements are then performed on this final state, generating records stored in classical memory. The machine learning model is trained using measurement records conditioned on \mathbf{x} and the model’s output would reconstruct the distribution of $|\psi_s\rangle$. The properties of unseen states conditioned on new \mathbf{x} such as fidelity can be obtained by post-processing the samples generated by the learned model.

states. Afterwards properties of the quantum states can be recovered by sampling from the model’s output and necessarily post-processing.

In auto-regressive models, each qubit is conditioned on the states of previously modeled qubits, introducing an inherent bias due to the imposed order. While this method works well in domains where data naturally follows a sequential structure, such as language (Yang et al., 2019; Brown et al., 2020) or time series (Hewamalage et al., 2021), it comes with a significant limitation when applied to quantum systems, where qubit interactions are *non-sequential* and the complex entanglement does not adhere to a predefined order. Based on our experimental results, the reliance on sequential modeling could lead to oversimplified representations of the entanglement structure, limiting the model’s ability to fully capture the intricate correlations between qubits. Consequently, modeling quantum systems with sequential dependencies introduces biases that may fail to capture the true complexity of the entanglement and correlations, leading to suboptimal estimations of quantum properties.

To address these challenges, we propose **QuaDiM (Quantum state property estimation using Diffusion Models)**, a novel *non-autoregressive* generative model based on diffusion models (Ho et al., 2020; Dhariwal & Nichol, 2021; Song et al., 2021a;c). Unlike auto-regressive approaches, QuaDiM treats all qubits equally without imposing a predefined order, thereby avoiding potential biases. The model learns a mapping from physical variables, i.e. the parameters of a system’s Hamiltonian, to the ground-state properties associated with those variables. Once trained, QuaDiM is capable of generalizing to previously unseen quantum systems, allowing it to predict quantum state properties for systems not encountered during training. This generalization capability is particularly valuable in practical scenarios where the quantum states of interest may cannot be prepared on modern noisy intermediate-scale quantum (NISQ) hardware, or quantum states difficult to simulated classically.

The underlying mechanism of QuaDiM is rooted in diffusion models, which iteratively denoise Gaussian noise to generate samples from the target distribution (Austin et al., 2021; Kong et al., 2021). In contrast with auto-regressive models, QuaDiM offers an advantage by treating all qubits equally throughout the denoising process, encouraging to remove the need for any predefined ordering of qubits. Mathematically, QuaDiM initiates from a random Gaussian distribution, which is progressively refined through a series of denoising steps to approximate the true distribution of the quantum state. This iterative process facilitates QuaDiM to capture correlations between qubits more effectively and without the biases introduced by a sequential models. By incrementally learning to reverse the noise process, the model naturally handles the complex interactions and entanglements inherent in many-body quantum systems. As a result, QuaDiM not only achieves higher accuracy in QPE but also demonstrates scalability when applied to large-scale systems up to 100 qubits. The model’s iterative refinement mechanism encourages that all parts of the system are considered simultaneously, with the hope of being helpful for estimating properties like correlation and entanglement entropy, where the relationships between all qubits are equally important.

We validate the efficacy of QuaDiM through extensive numerical experiments on predicting the correlation and entanglement entropy of the 1D anti-ferromagnetic Heisenberg model with up to 100

108 qubits. The results show that QuaDiM outperforms baselines, especially auto-regressive approaches,
 109 in scenarios with limited training measurements data and reduced sample complexity. QuaDiM’s
 110 ability to handle these challenging conditions highlights its potential for practical applications in
 111 quantum computing and related areas, where resource constraints and data scarcity are prevalent.

112 **Our contributions.** 1) We introduce QuaDiM, the first-ever (to the best of our knowledge) non-
 113 autoregressive conditional generative model for QPE. By utilizing diffusion models, QuaDiM iteratively
 114 denoises Gaussian noise to accurately approximate the distribution of unknown quantum states
 115 from limited measurements, encouraging equal and unbiased treatment of all qubits. 2) We classically
 116 simulate relatively large-scale quantum systems with up to 100 qubits to generate extensive training
 117 and test datasets for evaluation, showing QuaDiM’s scalability and practical applicability. 3) We
 118 conduct experiments on QPE tasks involving the prediction of correlation and entanglement entropy.
 119 Our results show that QuaDiM achieves lower prediction errors compared to baselines, particularly
 120 outperforming auto-regressive models such as Carrasquilla et al. (2019) and Tang et al. (2024).

121 2 RELATED WORK AND PRELIMINARIES

122 **Learning-based Quantum State Property Estimation.** In the domain of learning-based QPE,
 123 autoregressive models such as RNN-based (Carrasquilla et al., 2019; Hibat-Allah et al., 2020),
 124 CNN-based (Wu et al., 2019; Sharir et al., 2020), and transformer-based models (Cha et al., 2021;
 125 Wang et al., 2022; Du et al., 2023; Tang et al., 2024) have been extensively explored. These models
 126 inherently assume a sequential ordering of qubits, introducing biases that could limit their ability
 127 to capture the complex entanglement and correlations in quantum systems where qubits interact
 128 non-sequentially. This sequential dependency may lead to oversimplified representations of the
 129 entanglement structure, hindering accurate property estimation.

130 Alternatively, generative models that learn variational wave functions—such as those based on
 131 deep Boltzmann machines (DBMs) (Gao & Duan, 2017; Nomura et al., 2017), variational autoen-
 132 coders (VAEs) (Rocchetto et al., 2018), and generative adversarial networks (GANs) (Ahmed et al.,
 133 2021)—have been proposed to represent quantum states. While capable of capturing complex proba-
 134 bility distributions, these models typically learn representations for a single specific quantum state and
 135 lack the ability to generalize to unseen states, restricting their applicability in predicting properties
 136 of new quantum systems. Although GANs (Ahmed et al., 2021) could, in principle, generalize to
 137 unknown quantum states, their learning objective involves reconstructing the density matrix. This
 138 significantly hinders scalability because the complexity of fully describing a density matrix increases
 139 exponentially w.r.t quantum system size, making such approaches impractical for large-scale systems.
 140 Moreover, recent efforts have proposed representing quantum states using diffusion models (Zhu
 141 et al., 2024). However, this work requires direct access to the density matrix of quantum states as
 142 input and the experiments are only performed on relatively small quantum systems with 4 qubits,
 143 which is impractical for the NISQ devices with hundreds or thousands of qubits. This fundamental
 144 limitation hampers the feasibility of applying these techniques to real-world quantum systems.

145 **Quantum State and Quantum Measurement.** A quantum bit, or *qubit*, serves as the fundamental
 146 unit in quantum systems. The collection of all qubits within a (sub)system constitutes the *quantum*
 147 *state*. Prior to measurement, a qubit exists in a superposition of states, but upon measurement, it
 148 collapses into a definite state. The mathematical representation of a quantum state depends on the
 149 choice of basis states. For instance, using the orthogonal *computational basis states* $|0\rangle = \begin{bmatrix} 1 \\ 0 \end{bmatrix}$ and
 150 $|1\rangle = \begin{bmatrix} 0 \\ 1 \end{bmatrix}$, a single qubit can be expressed as a linear combination $|\phi\rangle = \alpha|0\rangle + \beta|1\rangle = \begin{bmatrix} \alpha \\ \beta \end{bmatrix}$ in
 151 the complex vector space \mathbb{C}^2 , where $\alpha, \beta \in \mathbb{C}$ are complex amplitudes satisfying the normalization
 152 condition $|\alpha|^2 + |\beta|^2 = 1$. An alternative representation of a quantum state employs the *density*
 153 *operator* or *density matrix*. For example, the density matrix corresponding to $|0\rangle$ is given by
 154 $\rho_0 = |0\rangle\langle 0| = \begin{pmatrix} 1 & 0 \\ 0 & 0 \end{pmatrix}$, where $\langle 0|$ denotes the conjugate transpose of $|0\rangle$.

155 A general quantum state comprising L qubits can be represented by a *wave function*:

$$156 |\psi\rangle = \sum_{\sigma_1=1}^K \cdots \sum_{\sigma_L=1}^K \Psi(\sigma_1, \dots, \sigma_L) |\sigma_1, \dots, \sigma_L\rangle, \quad (1)$$

157 where $\Psi : \mathbb{Z}^L \rightarrow \mathbb{C}$ assigns a complex amplitude to each fixed configuration $\sigma = (\sigma_1, \dots, \sigma_L)$ of
 158 the L qubits, satisfying the normalization condition $\sum_{\sigma_1=1}^K \cdots \sum_{\sigma_L=1}^K |\Psi(\sigma_1, \dots, \sigma_L)|^2 = 1$. Each
 159 $\sigma_i \in \{1, \dots, K\}$ represents one of the K possible outcomes when a measurement is performed on
 160
 161

the i -th qubit. The wave function resides in a complex Hilbert space, with the vector representation $|\psi\rangle \in \mathbb{C}^{K^L}$ and its density matrix $|\psi\rangle\langle\psi| \in \mathbb{C}^{K^L \times K^L}$, both of which grow exponentially large with increasing L . In this paper, we consider the Pauli-6 measurements such that $K = 6$.

Quantum measurements translate aspects of quantum information into classical data for subsequent processing, utilizing a set of *measurement operators* $\{\mathbf{O}_k\}_{k=1}^K$ that satisfy the completeness relation $\sum_k \mathbf{O}_k = \mathbf{I}$, where K denotes the total number of possible outcomes. Measuring a qubit yields different results corresponding to the indices k of the measurement operators. Specifically, for a quantum state ρ , the probability of obtaining outcome k upon measurement is $p(k) = \text{tr}(\rho \mathbf{O}_k)$. In systems with L qubits, it is common practice to perform measurements on all qubits simultaneously or in *parallel* (Leibfried et al., 1996; Jullien et al., 2014). According to Born’s rule (Born, 1926) in quantum mechanics, this measurement process produces a string of outcomes $\sigma = (\sigma_1, \dots, \sigma_L)$, where each $\sigma_i \in \{1, \dots, K\}$, with probability $|\Psi(\sigma_1, \dots, \sigma_L)|^2$ as defined in Eq. 1.

Diffusion Models. Diffusion models are a class of generative models that have gained significant attention in recent years due to their ability to produce high-quality samples from complex distributions (Ho et al., 2020; Song et al., 2021a). These models typically consist of two main processes: a forward process that gradually adds noise to the data, and a reverse process that aims to reconstruct the original data from the noisy representation. In the forward process, a data point sampled from a real-world distribution, denoted as $\mathbf{z}_0 \sim p(\mathbf{z})$, is progressively corrupted by adding Gaussian noise. This process transforms \mathbf{z}_0 into a standard Gaussian noise vector $\mathbf{z}_T \sim \mathcal{N}(0, \mathbf{I})$ over a predefined number of steps T . For each step $t \in \{1, 2, \dots, T\}$, the perturbation is governed by the conditional distribution $p(\mathbf{z}_t | \mathbf{z}_{t-1}) = \mathcal{N}(\mathbf{z}_t; \sqrt{1 - \beta_t} \mathbf{z}_{t-1}, \beta_t \mathbf{I})$, where $\beta_t \in (0, 1)$ represents varying variance scales at each time step. This formulation allows for a controlled degradation of the original data, enabling the model to learn to navigate through the noise space effectively. Once the forward process is complete, the reverse denoising process seeks to recover the original data \mathbf{z}_0 by sampling from \mathbf{z}_T . This is achieved through the training of a diffusion model f_θ , which learns the conditional distributions necessary to reverse the noise addition process. The learning objective typically involves minimizing the difference between the predicted and actual distributions, often through techniques such as score matching (Song et al., 2021b) or variational inference (Sohl-Dickstein et al., 2015). Diffusion models have demonstrated remarkable capabilities in generating high-fidelity samples across various domains, including image synthesis (Rombach et al., 2022), audio generation (Kong et al., 2021), and more recently, applications in solving combinatorial optimization problems (Li et al., 2024) and imitation learning (Pearce et al., 2023). Their inherent flexibility and robustness also make them an ideal candidate for capturing the complex distributions associated with quantum systems, thus paving the way for advancements in quantum machine learning applications.

Classical Shadow for Post-Processing. A standalone generative model and the samples drawn from its distribution cannot directly reconstruct a quantum state or extract certain features of it. Post-processing is necessary. In this paper, we consider using classical shadow (Huang et al., 2020) based on randomized single-qubit measurements to predict quantum state properties. This measurement procedure is highly efficient on both quantum experiments and classical simulations. Accordingly, we employ Pauli-6 positive operator-valued measure (POVM) to collect discrete measurement records, which are used to train the generative model. Concretely, the Pauli-6 POVM is given as $O_{\text{Pauli-6}} = \{\frac{1}{3} \times |0\rangle\langle 0|, \frac{1}{3} \times |1\rangle\langle 1|, \frac{1}{3} \times |+\rangle\langle +|, \frac{1}{3} \times |-\rangle\langle -|, \frac{1}{3} \times |r\rangle\langle r|, \frac{1}{3} \times |l\rangle\langle l|\}$, where $\{|0\rangle, |1\rangle\}$, $\{|+\rangle, |-\rangle\}$, $\{|r\rangle, |l\rangle\}$ stand for the eigenbasis of the Pauli operators Z, X , and Y , respectively. Suppose that the quantum system has L qubits, measuring a single qubit using $O_{\text{Pauli-6}}$ leads to a snapshot $\hat{\rho}_i^{(m)} = 3|s_i^{(m)}\rangle\langle s_i^{(m)}| - \mathbf{I}$ where $i \in \{1, \dots, L\}$ denotes the i -th qubit and $m \in \{1, \dots, M\}$ denotes the m -th measurement. Then the quantum state properties such as correlation and the entanglement entropy can be estimated using the LM snapshots. The details can be found in Sec. 4. After the learning model have been trained, we sample from the model’s distribution conditioned on the unseen parameters and collect the samples, i.e., the measurement data. Then classical shadow is used for post-processing to estimate the properties of unknown quantum states and the results are compared to the ground truth to evaluate the model’s performance.

3 METHODOLOGY

We first define the task of QPE in Sec. 3.1. Key methods and insights underlying QuaDiM are then detailed in Sec. 3.2, where we discuss its mathematical foundations and core innovations.

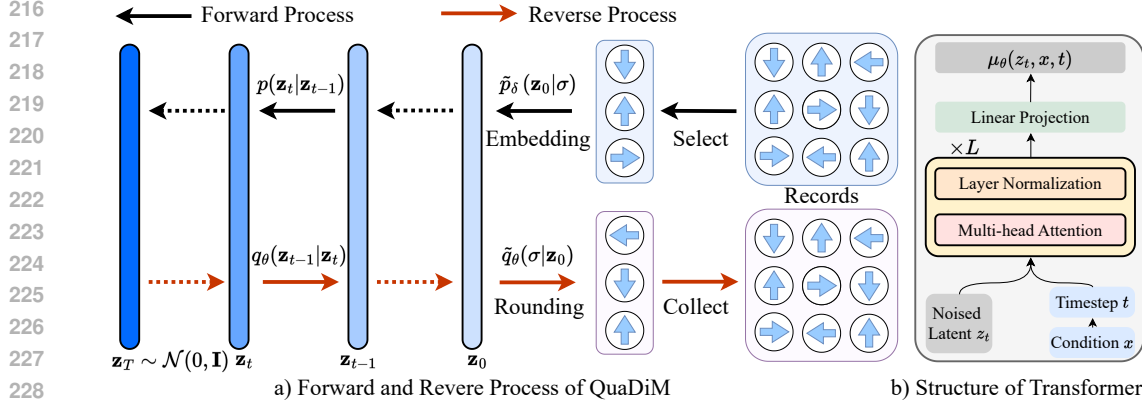


Figure 2: **a)** The diffusion forward process iteratively perturbs the input by adding Gaussian noise, while the reverse process incrementally removes the noise to recover the original distribution. To facilitate the transition between the latent variable \mathbf{z}_0 and the observed records σ , an embedding function (Li et al., 2022) is employed, along with a rounding step (Gong et al., 2023). **b)** The main learnable part is a multi-layer transformer. It models the mean of the posterior distribution q_θ .

3.1 PROBLEM DEFINITION

The problem is to learn to predict the quantum state properties of ground states of parameterized Hamiltonians. We consider a family of Hamiltonians, where the Hamiltonian $H(\mathbf{x})$ is parameterized by a set of real parameters $\mathbf{x} \in \mathbb{R}^p$. These parameters are physical condition variables determining the evolution dynamics of the quantum system. Different physical conditions could lead to different ground states. The neural network is trained on training data consisting of sampled values of $\{\mathbf{x}_i\}_{i=1}^{N^{tr}}$, each accompanied by the corresponding measurement records $\mathbf{R}_i \in \mathbb{Z}^{M_{in} \times L}$ obtained from Pauli-6 measurements repeatedly operated M_{in} times on the ground state $\rho(\mathbf{x}_i)$ of $H(\mathbf{x}_i)$. This training data could be obtained from either classical simulations or quantum experiments. During the inference phase, we sample M_{out} times from the trained neural network conditioned on a new values of $\mathbf{x}^* \in \{\mathbf{x}_i\}_{i=1}^{N^{te}}$ in the test data and outputs a collection of measurement data $\mathbf{R}^* \in \mathbb{Z}^{M_{out} \times L}$ of the unknown quantum state $\rho(\mathbf{x}^*)$. Ground state properties can then be estimated using post-processing on the \mathbf{R}^* such as the classical shadow.

3.2 QUADIM

We propose QuaDiM to extend vanilla diffusion models to learn conditional quantum state representations (as shown in Fig. 2), concerning the architecture and the training objective. For conciseness if not otherwise specified, we will omit the subscripts of the variables in the subsequent text.

3.2.1 FORWARD NOISING PROCESS WITH QUADIM

Although diffusion models have achieved success in image generation, applying continuous diffusion models to inherently discrete quantum measurement records remains non-trivial. We follow the Diffusion-LM (Li et al., 2022) in the text generation domain to design an embedding function that projects discrete measurement records into a high-order continuous feature space. Specifically, given a physical condition \mathbf{x} and the corresponding measurement records \mathbf{R} , QuaDiM first randomly samples a measurement string $\sigma = (\sigma_1, \dots, \sigma_L)$ which is a single row of \mathbf{R} . To apply a continuous diffusion model to discrete measurements, a token embedding function $\text{EMB}(\sigma_l)$ is introduced to map the single-qubit measurement outcome σ_l to a d -dimensional vector for each $l \in \{1, \dots, L\}$. The token embeddings are jointly trained with diffusion model’s parameters. We empirically find that these learnable embeddings can achieve better numerical results than the fixed embeddings. The token embedding is accompanied with trainable positional embedding (PE) with the same hidden dimension d . Thus the token embedding function is written as $\text{EMB}(\sigma) = [\text{EMB}(\sigma_1) + \text{PE}(1), \dots, \text{EMB}(\sigma_L) + \text{PE}(L)] \in \mathbb{R}^{L \times d}$. The initial input to the diffusion model in time step $t = 0$ is an additional Markov transition from $\text{EMB}(\sigma)$, given as

$$\tilde{p}_\delta(\mathbf{z}_0|\sigma) = \mathcal{N}(\mathbf{z}_0; \text{EMB}(\sigma), \beta_0 I), \quad (2)$$

where δ is the set of parameters of learnable token embeddings and positional embeddings. The forward noising process gradually corrupts \mathbf{z}_0 into a standard Gaussian noise $\mathbf{z}_T \sim \mathcal{N}(0, \mathbf{I})$. For each time step $t \in \{1, \dots, T\}$, the perturbation is defined as $p(\mathbf{z}_t|\mathbf{z}_{t-1}) = \mathcal{N}(\mathbf{z}_t; \sqrt{1 - \beta_t}\mathbf{z}_{t-1}, \beta_t \mathbf{I})$.

3.2.2 REVERSE CONDITIONAL DENOISING PROCESS WITH QUADIM

The proposed conditional denoising employs a classifier-free approach, i.e. we do not need to train an additional classifier to navigate the denoising process. Instead of performing conditional denoising directly on the discrete quantum measurement records, we perform it on the sequence of continuous latent variables $\mathbf{z}_{0:T}$ defined by the QuaDiM. It enables a simple gradient-based algorithm to perform complex, controllable quantum state generation based on diffusion models. Specifically, conditional denoising is equivalent to decoding from the posterior $q_{\theta}(\mathbf{z}_{0:T}|\mathbf{x}) = q(\mathbf{z}_T) \prod_{t=1}^T q_{\theta}(\mathbf{z}_{t-1}|\mathbf{z}_t, \mathbf{x})$. For each denoising step, we model it as a Gaussian $q_{\theta}(\mathbf{z}_{t-1}|\mathbf{z}_t, \mathbf{x}) = \mathcal{N}(\mathbf{z}_{t-1}; \mu_{\theta}(\mathbf{z}_t, \mathbf{x}, t), \gamma(t)\mathbf{I})$, where μ_{θ} and $\gamma(t)$ are the predicted mean and variance:

$$\mu_{\theta}(\mathbf{z}_t, \mathbf{x}, t) = \frac{\bar{\beta}_{t-1}\sqrt{1-\beta_t}}{\beta_t}\mathbf{z}_t + \frac{\beta_t\sqrt{1-\bar{\beta}_{t-1}}}{\bar{\beta}_t}f_{\theta}(\mathbf{z}_t, \mathbf{x}, t), \quad \gamma(t) = \frac{\beta_t\bar{\beta}_{t-1}}{\bar{\beta}_t}, \quad (3)$$

where $\bar{\beta}_t = 1 - \prod_{i=1}^t(1 - \beta_i)$. The network $\mu_{\theta}(\mathbf{z}_t, \mathbf{x}, t)$ is akin to the multi-layer transformer decoder (Vaswani et al., 2017). The distinction is that an additional time step embedding is specified by the transformer sinusoidal position embedding (PE) (Ho et al., 2020). Besides, to achieve the controllable generation of quantum states conditioned on the physical variable \mathbf{x} , we use a feed-forward network (FFN) with one hidden layer to transform \mathbf{x} into a hidden feature with the same dimension d . This feature is viewed as a global information added to the token embeddings of measurement records, such that the input to the transformer at time step t is $\mathbf{H}^0 = \mathbf{z}_t + \text{PE}(t) + \text{FFN}(\mathbf{x})$. Suppose that the $(l-1)$ -th layer’s output $\mathbf{H}^{l-1} \in \mathbb{R}^{L \times d}$ where d is the hidden dimension, we have:

$$\begin{aligned} \mathbf{H}^l &= \text{MULTIHEADATTENTION}(\mathbf{H}^{l-1}) = \llbracket \mathbf{O}_1^l, \dots, \mathbf{O}_h^l \rrbracket \mathbf{W}_o^l, \\ \text{with } \mathbf{O}_j^l &= \frac{(\mathbf{H}^{l-1} \mathbf{W}_{q,j}^l)(\mathbf{H}^{l-1} \mathbf{W}_{k,j}^l)^{\top}}{\sqrt{d}} \mathbf{H}^{l-1} \mathbf{W}_{v,j}^l, \end{aligned} \quad (4)$$

where $\llbracket \cdot \rrbracket$ denotes the concatenation operation, $\mathbf{W}_{q,j}^l, \mathbf{W}_{k,j}^l, \mathbf{W}_{v,j}^l \in \mathbb{R}^{d \times d/h}$ and $\mathbf{W}_o^l \in \mathbb{R}^{d \times d}$ are the parameters to be learned. In this paper, all the experimental results of QuaDiM are reported for a transformer configuration consisting of 4 heads, 4 layers, and 128 hidden dimensions. The maximum denoising time steps is set to $T = 2000$.

3.2.3 LEARNING OBJECTIVE

The canonical learning objective is to minimize the KL divergence between the joint probability distribution $p(\mathbf{z}_{0:T}|\sigma)$ and $q_{\theta}(\mathbf{z}_{0:T}|\mathbf{x})$ corresponding to the forward and reverse processes defined by the diffusion model, respectively. The objective is given as

$$\mathcal{L}_{KL} = \mathbb{E}_{p(\mathbf{z}_{0:T}|\sigma)} \log \frac{p(\mathbf{z}_{0:T}|\sigma)}{q_{\theta}(\mathbf{z}_{0:T}|\mathbf{x})}, \quad (5)$$

where $p(\mathbf{z}_{0:T}|\sigma) = \tilde{p}_{\delta}(\mathbf{z}_0|\sigma) \prod_{t=1}^T p(\mathbf{z}_t|\mathbf{z}_{t-1})$ denotes the distribution of the forward process, and $q_{\theta}(\mathbf{z}_{0:T}|\mathbf{x}) = q(\mathbf{z}_T) \prod_{t=1}^T q_{\theta}(\mathbf{z}_{t-1}|\mathbf{z}_t, \mathbf{x})$ represents the distribution of the reverse process. Note that in the forward process, $\tilde{p}_{\delta}(\mathbf{z}_0|\sigma)$ is the Markov transition (as given in Eq. 2) from the discrete quantum measurements to their continuous embeddings, allowing the token embeddings and model parameters to jointly participate in gradient descent. The objective can be further simplified to

$$\mathcal{L}_{KL} = \mathbb{E}_{p(\mathbf{z}_{0:T}|\sigma)} \left[\log \frac{p(\mathbf{z}_T|\mathbf{z}_0)}{q(\mathbf{z}_T)} + \sum_{t=2}^T \log \frac{p(\mathbf{z}_{t-1}|\mathbf{z}_0, \mathbf{z}_t)}{q_{\theta}(\mathbf{z}_{t-1}|\mathbf{z}_t)} + \log \frac{\tilde{p}_{\delta}(\mathbf{z}_0|\sigma)}{q_{\theta}(\mathbf{z}_0|\mathbf{z}_1)} \right]. \quad (6)$$

The detailed derivation and explanation of each term are given in Appendix A. In the reverse process, the diffusion model iteratively removes Gaussian noise \mathbf{z}_T and outputs the embeddings \mathbf{z}_0 . To estimate the reconstruction quality from the model’s output distribution when training the model, a rounding step (Li et al., 2022; Gong et al., 2023) is added to map the continuous \mathbf{z}_0 obtained from the denoising process back to discrete measurement outcomes σ of length L . Specifically, the step is given as $\tilde{q}_{\theta}(\sigma|\mathbf{z}_0) = \prod_{l=1}^L \tilde{q}_{\theta}(\sigma_l|\mathbf{z}_{0,l})$ and $\mathbf{z}_{0,l}$ is the l -th component of $\mathbf{z}_0 \in \mathbb{R}^{L \times d}$. Now we introduce the overall objective as the combination of two terms: maximizing the average negative log-likelihood $\mathbb{E}_{p(\mathbf{z}_0|\mathbf{x}, \mathbf{z}_{1:T})} \log \tilde{q}_{\theta}(\sigma|\mathbf{z}_0)$ and minimizing the KL divergence \mathcal{L}_{KL} . Thus the objective is as follows, where the detailed derivation is given in Appendix B.

$$\begin{aligned} \min_{\delta, \theta} \mathcal{L} &= \min_{\delta, \theta} [\mathcal{L}_{KL} - \mathbb{E}_{p(\mathbf{z}_0|\mathbf{x}, \mathbf{z}_{1:T})} \log \tilde{q}_{\theta}(\sigma|\mathbf{z}_0)] \\ &= \min_{\delta, \theta} \mathbb{E}_{\mathbf{x} \in \{\mathbf{x}_i\}} \left[\|\text{EMB}(\sigma) - \mu_{\theta}(\mathbf{z}_1, \mathbf{x}, 1)\|^2 + \sum_{t=2}^T \|\mathbf{z}_0 - \mu_{\theta}(\mathbf{z}_t, \mathbf{x}, t)\|^2 - \log \tilde{q}_{\theta}(\sigma|\mathbf{z}_0) \right], \end{aligned} \quad (7)$$

Table 1: RMSE of predicting the correlations of all subsystems of size two on the test dataset. The result is averaged over Heisenberg model instances and each pair of adjacent qubits. For CS, M denotes the number of input measurements. While for the neural network-based approaches M denotes the number of sampled measurements M_{out} from trained models. The best results are emphasized in **red** while the second-best results are distinguished in **blue**.

Method	$L = 10$				$L = 40$				$L = 70$				$L = 100$			
	$M = 100$	1000	10000	20000	100	1000	10000	20000	100	1000	10000	20000	100	1000	10000	20000
CS	0.1564	0.0509	0.0156	0.0107	0.1696	0.0538	0.0173	0.0121	0.1771	0.0545	0.0172	0.0121	0.1724	0.0547	0.0172	0.0122
RBFK		0.0796				0.0639				0.0578				0.0493		
NTK		0.0775				0.0622				0.0565				0.0470		
RNN	0.1328	0.0502	0.0145	0.0119	0.1795	0.0671	0.0164	0.0118	0.2137	0.0739	0.0240	0.0153	0.2325	0.0806	0.0251	0.0163
LLM4QPE	0.1316	0.0489	0.0136	0.0093	0.1624	0.0513	0.0142	0.0097	0.1814	0.0527	0.0155	0.0116	0.1759	0.0531	0.0152	0.0114
Ours	0.1269	0.0432	0.0097	0.0085	0.1582	0.0465	0.0113	0.0091	0.1679	0.0473	0.0117	0.0092	0.1686	0.0478	0.0125	0.0098

4 EXPERIMENTS

In this section, we first introduce dataset construction and baselines in Sec. 4.1 and Sec. 4.2. In Sec. 4.3 and Sec. 4.4, we evaluate QuaDiM’s performance on QPE tasks compared to state-of-the-art baselines, focusing on predicting correlation and entanglement entropy in various system sizes.

4.1 DATASETS

We focus on investigating the ground state of the one-dimensional anti-ferromagnetic Heisenberg model, as it can be efficiently simulated classically at relatively large scale. Its Hamiltonian is parameterized by $\mathbf{x} \in \mathbb{R}^{L-1}$ and can be written as

$$H(\mathbf{x}) = \sum_i x_i (X_i X_{i+1} + Y_i Y_{i+1} + Z_i Z_{i+1}), \quad (8)$$

where L is the number of qubits and \mathbf{x} is a sequence of real numbers for the coupling strength among qubits. X, Y, Z denotes the Pauli operator and X_i indicates that Pauli X is operated on the i -th qubit.

For the sake of simplicity, we first describe how a single sample is generated, with other samples in the dataset being produced in a similar manner. Given the length L of the quantum system, we first randomly sample $L - 1$ distinct values of \mathbf{x} to construct the corresponding Hamiltonian $H(\mathbf{x})$. We then obtain the ground state of the $H(\mathbf{x})$ using classical simulation based on tensor networks (Fishman et al., 2022). Thanks to the efficiency of tensor networks, we are able to simulate quantum systems from 10 to 100 qubits on a CPU cluster. Subsequently, Pauli-6 positive operator-valued measure (POVM) is utilized to measure the ground state corresponding to $H(\mathbf{x})$ and the output is a string-like sequence $\boldsymbol{\sigma} = (\sigma_1, \dots, \sigma_L)$ where $\sigma_l \in \{1, 2, \dots, K\}$. The same measurement procedure is performed M_{in} times independently on the M_{in} copies of the ground state. As a result, the model input consists of \mathbf{x} along with the corresponding measurement records $\mathbf{R} \in \mathbb{Z}^{M_{in} \times L}$. The above process is repeated N^{tr} and N^{te} times to obtain the training dataset $\{\mathbf{x}_i\}_{i=1}^{N^{tr}}$ with measurement records $\{\mathbf{R}_i\}_{i=1}^{N^{tr}}$ and test dataset $\{\mathbf{x}_j\}_{j=1}^{N^{te}}$ with $\{\mathbf{R}_j\}_{j=1}^{N^{te}}$.

As for the ground truth labels, which represent the ground state properties of the Hamiltonian $H(\mathbf{x})$ such as correlation and entanglement entropy, we utilize exact diagonalization (Weiße & Fehske, 2008) for quantum systems with $L \leq 10$ to obtain the true labels. For quantum systems with $L > 10$, we collect a substantial amount of measurement data by setting $M = 320,000$ and approximate the corresponding labels using classical shadow (Huang et al., 2020).

4.2 BASELINES

We consider the classical shadow (CS) (Huang et al., 2020) – a SOTA learning-free protocol for constructing the representation of an unknown quantum state. For learning-based baselines, we consider kernel methods including the Radial Basis Function Kernel (RBFK) and Neural Tangent Kernel (NTK) implemented in Huang et al. (2022). We also explore advanced deep learning approaches, including a Recurrent Neural Network (RNN)-based model (Carrasquilla et al., 2019), and a transformer-based SOTA model LLM4QPE (Tang et al., 2024).

For all the methods, we set $N^{tr} = 100$ and $N^{te} = 20$, with the number of qubits in the quantum system $L \in \{10, 40, 70, 100\}$. To construct the training set, we perform repeated measurements of $M_{in} = 1000$ for each ground state. To evaluate the performance of the trained QuaDiM and auto-regressive baselines in predicting certain quantum state property w.r.t. different sampling counts, the model is sampled M_{out} times, and the outputs are processed to predict the ground state property

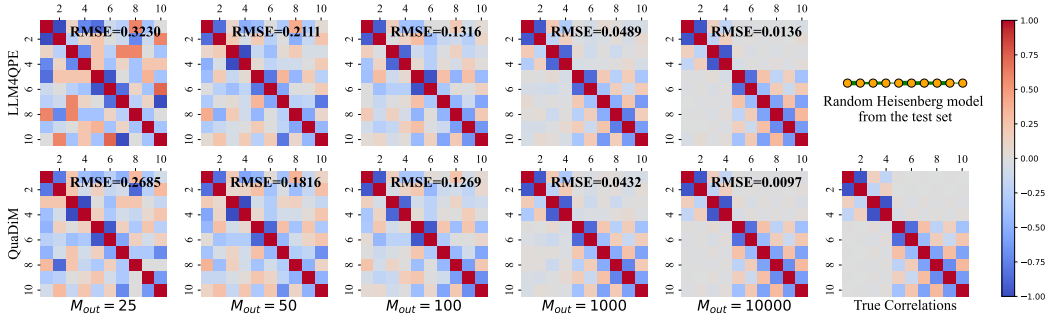


Figure 3: Visualization of predicted correlations \hat{C}_{ij} for the ground state of the 1D anti-ferromagnetic Heisenberg model of length $L = 10$ with different number of samples M_{out} from the trained models. The chain in the upper right corner represents a Heisenberg model selected from the test set, where the width of the edges indicates the coupling strength x_i . The upper part shows the prediction results of LLM4QPE (Tang et al., 2024), while the lower part presents those of proposed QuaDiM alongside the ground truth. For all the settings, we fix $M_{in} = 1000$ and use classical shadow for post-processing.

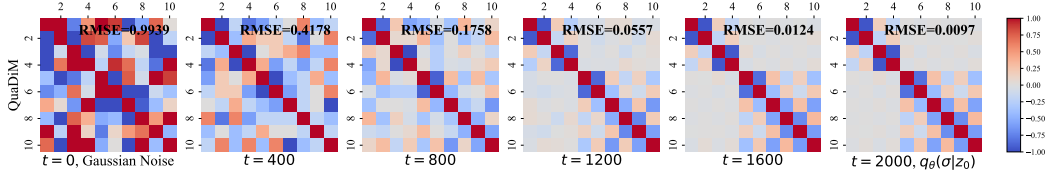


Figure 4: Visualization of predicted correlations of QuaDiM \hat{C}_{ij} for the ground state of the 1D anti-ferromagnetic Heisenberg model of length $L = 10$. The measurement samples are generated from the different denoising time step t . For all the settings, we fix $M_{in} = 1000$ and $M_{out} = 10000$.

of the Hamiltonian in the test dataset. We use the Root Mean Square Error (RMSE) to assess the difference between the predicted property and the true one, with smaller RMSE indicating that the model achieves better predictive accuracy with fewer measurement samples or sampling iterations. To adapt our proposed generative model, we made appropriate adjustments to all auto-regressive baselines including RNN and LLM4QPE, to facilitate generative training and sampling from the trained model, while employing the same classical shadow protocol for post-processing to ensure a fair comparison. For the kernel methods, since generative training is not possible, the model input retains only the physical condition \mathbf{x} . For specific details about baselines, please refer to Appendix D.

4.3 PREDICT THE CORRELATION

The first learning task is to predict the correlations of all subsystems of size two. Denote the density matrix of the quantum state as ρ . For two qubits located at different positions i and j , the correlation is described as $C_{ij} = \text{tr}(O_{ij}\rho)$ where $O_{ij} = \frac{1}{3}(X_i X_j + Y_i Y_j + Z_i Z_j)$. Given a physical condition \mathbf{x} , the model along with post-processing is learned to approximate the mapping $f: \mathbf{x} \rightarrow C_{ij}$.

The data sampled from the trained model will be fed into the classical shadow for post-processing. Specifically, assuming the number of samples is M_{out} , we obtain an output $R_{out} \in \mathbb{Z}^{M_{out} \times L}$, where each element can be converted into a snapshot $\hat{\rho}_i^{(m)} = 3|s_i^{(m)}\rangle\langle s_i^{(m)}| - \mathbf{I}$ where $i \in \{1, \dots, L\}$ and $m \in \{1, \dots, M_{out}\}$, as discussed in Sec. 2. Then the predicted correlation between the i -th qubit and the j -th qubit is calculated by

$$\hat{C}_{ij} = \frac{1}{3M_{out}} \sum_{o \in \{x, y, z\}} \sum_m^{M_{out}} \text{tr} \left[\left(\hat{\rho}_i^{(m)} \otimes \hat{\rho}_j^{(m)} \right) \left(\sigma_i^o \otimes \sigma_j^o \right) \right]. \quad (9)$$

As shown in Tab. 1, QuaDiM achieves the lowest RMSE across all the configurations, showcasing its ability to deliver precise correlation predictions even with a moderate M_{out} . An important advantage of QuaDiM is its ability to maintain excellent performance even with fewer M_{out} . For instance, at $M_{out} = 100$, QuaDiM’s RMSE of surpasses CS and remains competitive with the auto-regressive baselines. This trend persists across larger system sizes as well. QuaDiM demonstrates strong performance at low sample counts, indicating its efficiency in utilizing limited samples from the trained model for accurate quantum state property estimation.

As expected, the RMSE decreases with increasing M_{out} , reflecting that all models except for kernel methods improve in predictive accuracy as more measurement samples become available. However, the degree of improvement varies significantly between methods. The CS protocol performs reasonably well for small M_{out} but shows diminishing returns at larger M_{out} , particularly for larger system sizes ($L = 40$ and beyond). In contrast, QuaDiM continues to benefit from increased M_{out} , which suggests that the model is better at learning and generalizing from larger quantum systems.

Kernel-based methods (RBFK and NTK) show competitive performance for medium system sizes ($L = 40$), but they struggle to match the performance of the generative models (QuaDiM, LLM4QPE and RNN) at higher sample sizes or larger system sizes. This could be due to the inherent limitations of kernel methods in capturing the complex structure of large quantum systems, which generative models like QuaDiM can better model through learned representations.

One of the most critical challenges in quantum state estimation is scalability. While some methods, such as the classical shadow approach, demonstrate robust performance for smaller system sizes ($L = 10$), their performance becomes inferior compared to the neural network-based methods as L increases. This is consistent with the findings in [Huang et al. \(2022\)](#) that neural networks could more easily display non-local correlations, allowing in principle to capture quantum states with higher entanglement for relatively larger quantum systems. Notably, for $L = 100$, the RNN-based baseline yields significantly higher RMSE values compared to others, indicating that the auto-regressive training and generation mechanism makes oversimplified representations of the entanglement structure, limiting the model’s ability to fully capture the intricate correlations between qubits. Conversely, QuaDiM shows resilience to scaling, maintaining low RMSE values across all system sizes, with only a slight increase in RMSE as L increases. This scalability suggests that QuaDiM is particularly well-suited for handling large quantum systems, making it a promising approach for real-world quantum computations where the number of qubits can be extensive (for example, IBM’s latest commercial quantum computer has more than 1,000 qubits).

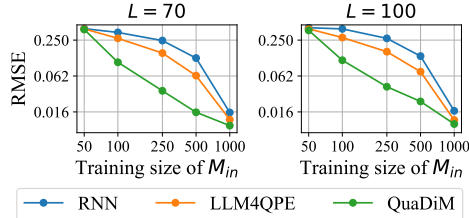


Figure 5: RMSE of predicting the correlations of all subsystems of size two on the test dataset of the auto-regressive baselines and the proposed QuaDiM for $L \in \{70, 100\}$. The models are trained using different number of input measurements M_{in} .

More results about the performance w.r.t. the samples complexity of the trained models. The experimental results visualized in Fig. 3 show the predicted correlations \hat{C}_{ij} for the ground state of the 1D anti-ferromagnetic Heisenberg model, with varying sample sizes M_{out} . QuaDiM outperforms the auto-regressive baseline LLM4QPE in achieving lower RMSE with fewer samples. As the sample size increases, QuaDiM continues to demonstrate superior performance, achieving an RMSE of 0.0097 at $M_{out} = 10000$, compared to LLM4QPE’s 0.0136. We also illustrate QuaDiM’s predicted correlations at various denoising time steps t in Fig. 4. As the denoising process progresses, the RMSE steadily decreases. This demonstrates that QuaDiM effectively reconstructs the distribution of quantum states as the denoising process advances, with each time step reducing the noise and improving the fidelity of the sampled quantum states. [A more fine-grained visualization of the prediction performance of QuaDiM is depicted in Fig. 6 in Appendix E.](#)

More results about the performance w.r.t. the number of measurements used for training. The experimental results shown in Fig. 5 highlight the predictive error of auto-regressive baselines and our proposed QuaDiM when predicting correlations for subsystems of size two within quantum systems of $L \in \{70, 100\}$. The models are trained using different numbers of input measurements M_{in} ranging from 50 to 1000. QuaDiM consistently outperforms the auto-regressive baselines across all training sizes. For both $L \in \{70, 100\}$, it achieves a lower RMSE with fewer input measurements compared to the other methods, showing an advantage in training efficiency. Notably, as M_{in} increases, QuaDiM’s RMSE decreases more sharply than that of the baselines, indicating that it can better approximate the (classical) probability distribution of quantum states using fewer input measurements. In quantum computation, where measurement resources are often limited for both quantum experiments and classical simulation ([Gebhart et al., 2023](#)), QuaDiM’s ability to perform well with fewer measurements offers a significant advantage over auto-regressive methods.

Table 2: RMSE of predicting the entanglement entropies of all subsystems of size two on the test dataset. The result is averaged over Heisenberg model instances and each pair of adjacent qubits. The best results are emphasized in red while the second-best results are distinguished in blue.

Method	$L = 10$				$L = 40$				$L = 70$				$L = 100$			
	$M = 100$	1000	10000	20000	100	1000	10000	20000	100	1000	10000	20000	100	1000	10000	20000
CS	0.5966	0.0922	0.0204	0.0119	0.6487	0.0927	0.0294	0.0259	0.6421	0.0943	0.0312	0.0298	0.6518	0.0998	0.0357	0.0316
RBFK		0.1268				0.1037				0.0997				0.0752		
NTK		0.1379				0.1034				0.0983				0.0719		
RNN	0.5225	0.1164	0.0187	0.0115	0.6132	0.1054	0.0246	0.0212	0.7948	0.1305	0.0514	0.0385	0.8229	0.1476	0.0617	0.0439
LLM4QPE	0.4937	0.0948	0.0176	0.0102	0.5878	0.0896	0.0223	0.0207	0.6258	0.0912	0.0276	0.0251	0.6392	0.1055	0.0312	0.0286
Ours	0.5479	0.0867	0.0132	0.0089	0.5629	0.0861	0.0187	0.0145	0.5970	0.0879	0.0245	0.0218	0.6125	0.0928	0.0281	0.0243

4.4 PREDICT THE ENTANGLEMENT ENTROPY

Another learning task is to predict the second-order Rényi entanglement entropy of the subsystem A , which is formulated as $E_A = -\log(\text{tr}(\rho_A^2))$, where A is a subsystem of the n -qubit quantum system. The required number of measurements scales exponentially in the size of the subsystem A , but is independent of total system size (Huang et al., 2020). In this paper, we consider learning the entanglement entropy of all the subsystems of size two. This leads to a local quadratic feature for a unknown quantum state ρ , which can be also efficiently estimated by the classical shadow given by

$$\begin{aligned}
 E_{ij} &= -\log(\text{tr}(\rho_{A_{ij}}^2)) = -\log(\text{tr}(\mathbf{S}_{A_{ij}}\rho \otimes \rho)) = -\log(\text{tr}(\mathbf{S}_{A_{ij}}\mathbb{E}[\hat{\rho}_1] \otimes \mathbb{E}[\hat{\rho}_2])) \\
 &\approx \frac{1}{M_{out}(M_{out} - 1)} \sum_{m \neq n} \text{tr}(\mathbf{S}_{A_{ij}}\hat{\rho}_1^{(m)} \otimes \hat{\rho}_2^{(n)}) = \hat{E}_{ij}, \quad (10)
 \end{aligned}$$

where $\hat{\rho}_1, \hat{\rho}_2$ are two independent snapshots of the unknown state ρ and $\mathbf{S}_{A_{ij}}$ denotes the local swap operator of two copies of the subsystem comprising the i -th and the j -th qubits. The $\mathbb{E}[\hat{\rho}]$ represents the averaged value among M_{out} samples from the trained model. Given a specific physical condition \mathbf{x} , the model along with post-processing is learned to approximate the mapping $f: \mathbf{x} \rightarrow E_{ij}$.

Tab. 2 compares models’ performance in predicting the entanglement entropy of subsystems of size two. The key metric is also the RMSE, with lower values indicating better predictive accuracy. The results are presented across different system size L and sample sizes M_{out} from the trained models. CS method performs reasonably well at lower system sizes and sample counts, but it struggles to maintain competitive RMSE values as both M and L increase. Similarly, the kernel-based methods demonstrate some degree of competitiveness but fall behind neural network-based models at larger system sizes and higher sample counts. It can be seen that QuaDiM achieves superior performance across most system sizes and sample counts, consistently achieving lower RMSE values compared to baseline models. This trend continues as the sample size increases, with QuaDiM maintaining its advantage over the other models. The RMSE reduction demonstrates that QuaDiM can accurately predict the entanglement entropy even with a relatively small number of samples.

Performance across system sizes. QuaDiM also scales effectively as the system size increases. This indicates that QuaDiM could be a practical choice for real-world quantum computations where the number of qubits can be large. The model’s ability to maintain low RMSE values across different system sizes shows its scalability even for the relative large quantum system with 100 qubits.

Sample efficiency from the trained models. One of the most important advantages of QuaDiM is its sample efficiency. It consistently achieves lower RMSE values with fewer samples for post-processing. As the number of samples increases, the performance gap widens, with QuaDiM achieving an RMSE of 0.0145 with $M_{out} = 20,000$, while LLM4QPE and CS exhibit higher RMSE. This sample efficiency is critical in post-processing, as large samples leads to prohibitive post-processing costs.

5 CONCLUSION

In this paper, we introduced QuaDiM, a novel non-autoregressive model for QPE based on diffusion models. Our results demonstrate it achieves superior performance in predicting quantum properties such as correlation and entanglement entropy with limited measurement data and reduced samples.

Limitations and Future Work. While QuaDiM demonstrates promising improvements, there is still room for further investigation regarding its scalability to highly entangled quantum systems and its sampling efficiency. Future work will aim to extend the model to accommodate more complex quantum systems and incorporate advanced methods to enhance the speed of diffusion sampling.

REFERENCES

- 540
541
542 Shah Nawaz Ahmed, Carlos Sánchez Muñoz, Franco Nori, and Anton Frisk Kockum. Quantum state
543 tomography with conditional generative adversarial networks. *Physical review letters*, 127(14):
544 140502, 2021.
- 545 Prabhanjan Ananth, Luowen Qian, and Henry Yuen. Cryptography from pseudorandom quantum
546 states. In *Annual International Cryptology Conference*, pp. 208–236. Springer, 2022.
- 547 Jacob Austin, Daniel D Johnson, Jonathan Ho, Daniel Tarlow, and Rianne Van Den Berg. Structured
548 denoising diffusion models in discrete state-spaces. *Advances in Neural Information Processing*
549 *Systems*, 34:17981–17993, 2021.
- 550 Thomas D Barrett, Aleksei Malyshev, and AI Lvovsky. Autoregressive neural-network wavefunctions
551 for ab initio quantum chemistry. *Nature Machine Intelligence*, 4(4):351–358, 2022.
- 552 Max Born. Quantenmechanik der stoßvorgänge. *Zeitschrift für physik*, 38(11-12):803–827, 1926.
- 553 Zvika Brakerski and Omri Shmueli. (pseudo) random quantum states with binary phase. In *Theory of*
554 *Cryptography Conference*, pp. 229–250. Springer, 2019.
- 555 Tom Brown, Benjamin Mann, Nick Ryder, Melanie Subbiah, Jared D Kaplan, Prafulla Dhariwal,
556 Arvind Neelakantan, Pranav Shyam, Girish Sastry, Amanda Askell, et al. Language models are
557 few-shot learners. *Advances in neural information processing systems*, 33:1877–1901, 2020.
- 558 Yudong Cao, Jonathan Romero, Jonathan P Olson, Matthias Degroote, Peter D Johnson, Mária
559 Kieferová, Ian D Kivlichan, Tim Menke, Borja Peropadre, Nicolas PD Sawaya, et al. Quantum
560 chemistry in the age of quantum computing. *Chemical reviews*, 119(19):10856–10915, 2019.
- 561 Giuseppe Carleo and Matthias Troyer. Solving the quantum many-body problem with artificial neural
562 networks. *Science*, 355(6325):602–606, 2017.
- 563 Juan Carrasquilla. Machine learning for quantum matter. *Advances in Physics: X*, 5(1):1797528,
564 2020.
- 565 Juan Carrasquilla, Giacomo Torlai, Roger G Melko, and Leandro Aolita. Reconstructing quantum
566 states with generative models. *Nature Machine Intelligence*, 1(3):155–161, 2019.
- 567 Peter Cha, Paul Ginsparg, Felix Wu, Juan Carrasquilla, Peter L McMahon, and Eun-Ah Kim.
568 Attention-based quantum tomography. *Machine Learning: Science and Technology*, 3(1):01LT01,
569 2021.
- 570 Zhuo Chen, Laker Newhouse, Eddie Chen, Di Luo, and Marin Soljatic. ANTN: Bridging autoregres-
571 sive neural networks and tensor networks for quantum many-body simulation. *Advances in neural*
572 *information processing systems*, 2023.
- 573 Marcus Cramer, Martin B Plenio, Steven T Flammia, Rolando Somma, David Gross, Stephen D
574 Bartlett, Olivier Landon-Cardinal, David Poulin, and Yi-Kai Liu. Efficient quantum state tomogra-
575 phy. *Nature communications*, 1(1):149, 2010.
- 576 G Mauro D’Ariano, Matteo GA Paris, and Massimiliano F Sacchi. Quantum tomography. *Advances*
577 *in imaging and electron physics*, 128:206–309, 2003.
- 578 Prafulla Dhariwal and Alexander Nichol. Diffusion models beat gans on image synthesis. *Advances*
579 *in neural information processing systems*, 34:8780–8794, 2021.
- 580 Yuxuan Du, Yibo Yang, Tongliang Liu, Zhouchen Lin, Bernard Ghanem, and Dacheng Tao. Shad-
581 ownet for data-centric quantum system learning. *arXiv preprint arXiv:2308.11290*, 2023.
- 582 Vedran Dunjko and Hans J Briegel. Machine learning & artificial intelligence in the quantum domain:
583 a review of recent progress. *Reports on Progress in Physics*, 81(7):074001, 2018.
- 584 Matthew Fishman, Steven R. White, and E. Miles Stoudenmire. The ITensor Software Library for Ten-
585 sor Network Calculations. *SciPost Phys. Codebases*, pp. 4, 2022. doi: 10.21468/SciPostPhysCodeb.
586 4. URL <https://scipost.org/10.21468/SciPostPhysCodeb.4>.

- 594 David Fitzek, Yi Hong Teoh, Hin Pok Fung, Gebremedhin A Dagne, Ejaaz Merali, M Schuyler
595 Moss, Benjamin MacLellan, and Roger G Melko. Rydberggpt. *arXiv preprint arXiv:2405.21052*,
596 2024.
- 597
- 598 Xun Gao and Lu-Ming Duan. Efficient representation of quantum many-body states with deep neural
599 networks. *Nature communications*, 8(1):662, 2017.
- 600
- 601 Valentin Gebhart, Raffaele Santagati, Antonio Andrea Gentile, Erik M Gauger, David Craig, Natalia
602 Ares, Leonardo Bianchi, Florian Marquardt, Luca Pezzè, and Cristian Bonato. Learning quantum
603 systems. *Nature Reviews Physics*, 5(3):141–156, 2023.
- 604
- 605 Shansan Gong, Mukai Li, Jiangtao Feng, Zhiyong Wu, and Lingpeng Kong. DiffuSeq: Sequence
606 to sequence text generation with diffusion models. In *International Conference on Learning
607 Representations*, 2023.
- 608
- 609 Hansika Hewamalage, Christoph Bergmeir, and Kasun Bandara. Recurrent neural networks for time
610 series forecasting: Current status and future directions. *International Journal of Forecasting*, 37
611 (1):388–427, 2021.
- 612
- 613 Mohamed Hibat-Allah, Martin Ganahl, Lauren E Hayward, Roger G Melko, and Juan Carrasquilla.
614 Recurrent neural network wave functions. *Physical Review Research*, 2(2):023358, 2020.
- 615
- 616 Jonathan Ho, Ajay Jain, and Pieter Abbeel. Denoising diffusion probabilistic models. *Advances in
617 neural information processing systems*, 33:6840–6851, 2020.
- 618
- 619 Hsin-Yuan Huang, Richard Kueng, and John Preskill. Predicting many properties of a quantum
620 system from very few measurements. *Nature Physics*, 16(10):1050–1057, 2020.
- 621
- 622 Hsin-Yuan Huang, Richard Kueng, Giacomo Torlai, Victor V Albert, and John Preskill. Provably
623 efficient machine learning for quantum many-body problems. *Science*, 377(6613):eabk3333, 2022.
- 624
- 625 Zhih-Ahn Jia, Biao Yi, Rui Zhai, Yu-Chun Wu, Guang-Can Guo, and Guo-Ping Guo. Quantum neural
626 network states: A brief review of methods and applications. *Advanced Quantum Technologies*, 2
627 (7-8):1800077, 2019.
- 628
- 629 T Jullien, P Roulleau, B Roche, A Cavanna, Y Jin, and DC Glattli. Quantum tomography of an
630 electron. *Nature*, 514(7524):603–607, 2014.
- 631
- 632 Abhinav Kandala, Antonio Mezzacapo, Kristan Temme, Maika Takita, Markus Brink, Jerry M Chow,
633 and Jay M Gambetta. Hardware-efficient variational quantum eigensolver for small molecules and
634 quantum magnets. *nature*, 549(7671):242–246, 2017.
- 635
- 636 Zhifeng Kong, Wei Ping, Jiaji Huang, Kexin Zhao, and Bryan Catanzaro. Diffwave: A versatile
637 diffusion model for audio synthesis. In *International Conference on Learning Representations*,
638 2021.
- 639
- 640 Dietrich Leibfried, DM Meekhof, BE King, CH Monroe, Wayne M Itano, and David J Wineland.
641 Experimental determination of the motional quantum state of a trapped atom. *Physical review
642 letters*, 77(21):4281, 1996.
- 643
- 644 Laura Lewis, Hsin-Yuan Huang, Viet T Tran, Sebastian Lehner, Richard Kueng, and John Preskill.
645 Improved machine learning algorithm for predicting ground state properties. *arXiv preprint
646 arXiv:2301.13169*, 2023.
- 647
- 648 Xiang Li, John Thickstun, Ishaan Gulrajani, Percy S Liang, and Tatsunori B Hashimoto. Diffusion-lm
649 improves controllable text generation. *Advances in Neural Information Processing Systems*, 35:
650 4328–4343, 2022.
- 651
- 652 Yang Li, Jinpei Guo, Runzhong Wang, and Junchi Yan. From distribution learning in training
653 to gradient search in testing for combinatorial optimization. *Advances in Neural Information
654 Processing Systems*, 36, 2024.

- 648 Cole Miles, Rhine Samajdar, Sepehr Ebadi, Tout T Wang, Hannes Pichler, Subir Sachdev, Mikhail D
649 Lukin, Markus Greiner, Kilian Q Weinberger, and Eun-Ah Kim. Machine learning discovery
650 of new phases in programmable quantum simulator snapshots. *Physical Review Research*, 5(1):
651 013026, 2023.
- 652 Michael A Nielsen and Isaac L Chuang. *Quantum computation and quantum information*. Cambridge
653 university press, 2010.
- 654
655 Yusuke Nomura, Andrew S Darmawan, Youhei Yamaji, and Masatoshi Imada. Restricted boltzmann
656 machine learning for solving strongly correlated quantum systems. *Physical Review B*, 96(20):
657 205152, 2017.
- 658 Tim Pearce, Tabish Rashid, Anssi Kanervisto, Dave Bignell, Mingfei Sun, Raluca Georgescu,
659 Sergio Valcarcel Macua, Shan Zheng Tan, Ida Momennejad, Katja Hofmann, and Sam Devlin.
660 Imitating human behaviour with diffusion models. In *The Eleventh International Conference on*
661 *Learning Representations*, 2023.
- 662
663 Andrea Rocchetto, Edward Grant, Sergii Strelchuk, Giuseppe Carleo, and Simone Severini. Learning
664 hard quantum distributions with variational autoencoders. *npj Quantum Information*, 4(1):28,
665 2018.
- 666 Robin Rombach, Andreas Blattmann, Dominik Lorenz, Patrick Esser, and Björn Ommer. High-
667 resolution image synthesis with latent diffusion models. In *Proceedings of the IEEE/CVF confer-*
668 *ence on computer vision and pattern recognition*, pp. 10684–10695, 2022.
- 669
670 Manas Sajjan, Junxu Li, Raja Selvarajan, Shree Hari Sureshababu, Sumit Suresh Kale, Rishabh Gupta,
671 Vinit Singh, and Sabre Kais. Quantum machine learning for chemistry and physics. *Chemical*
672 *Society Reviews*, 51(15):6475–6573, 2022.
- 673 Markus Schmitt and Markus Heyl. Quantum many-body dynamics in two dimensions with artificial
674 neural networks. *Physical Review Letters*, 125(10):100503, 2020.
- 675
676 Kristof T Schütt, Michael Gastegger, Alexandre Tkatchenko, K-R Müller, and Reinhard J Maurer.
677 Unifying machine learning and quantum chemistry with a deep neural network for molecular
678 wavefunctions. *Nature communications*, 10(1):5024, 2019.
- 679 Or Sharir, Yoav Levine, Noam Wies, Giuseppe Carleo, and Amnon Shashua. Deep autoregressive
680 models for the efficient variational simulation of many-body quantum systems. *Physical review*
681 *letters*, 124(2):020503, 2020.
- 682
683 Peter Shaw, Jakob Uszkoreit, and Ashish Vaswani. Self-attention with relative position representations.
684 *arXiv preprint arXiv:1803.02155*, 2018.
- 685
686 Jascha Sohl-Dickstein, Eric Weiss, Niru Maheswaranathan, and Surya Ganguli. Deep unsupervised
687 learning using nonequilibrium thermodynamics. In *International conference on machine learning*,
pp. 2256–2265. PMLR, 2015.
- 688
689 Jiaming Song, Chenlin Meng, and Stefano Ermon. Denoising diffusion implicit models. In *Intern-*
690 *ational Conference on Learning Representations*, 2021a.
- 691
692 Yang Song, Conor Durkan, Iain Murray, and Stefano Ermon. Maximum likelihood training of
693 score-based diffusion models. *Advances in neural information processing systems*, 34:1415–1428,
694 2021b.
- 695
696 Yang Song, Jascha Sohl-Dickstein, Diederik P Kingma, Abhishek Kumar, Stefano Ermon, and Ben
697 Poole. Score-based generative modeling through stochastic differential equations. In *International*
698 *Conference on Learning Representations*, 2021c.
- 699
700 Yehui Tang, Hao Xiong, Nianzu Yang, Tailong Xiao, and Junchi Yan. Towards llm4qpe: Unsuper-
701 vised pretraining of quantum property estimation and a benchmar. In *The Twelfth International*
Conference on Learning Representation, 2024.
- Giacomo Torlai and Roger G Melko. Machine-learning quantum states in the nisq era. *Annual Review*
of Condensed Matter Physics, 11:325–344, 2020.

702 Giacomo Torlai, Guglielmo Mazzola, Juan Carrasquilla, Matthias Troyer, Roger Melko, and Giuseppe
703 Carleo. Neural-network quantum state tomography. *Nature Physics*, 14(5):447–450, 2018.
704

705 Ashish Vaswani, Noam Shazeer, Niki Parmar, Jakob Uszkoreit, Llion Jones, Aidan N Gomez, Łukasz
706 Kaiser, and Illia Polosukhin. Attention is all you need. *Advances in neural information processing*
707 *systems*, 30, 2017.

708 Haoxiang Wang, Maurice Weber, Josh Izaac, and Cedric Yen-Yu Lin. Predicting properties of
709 quantum systems with conditional generative models. *arXiv preprint arXiv:2211.16943*, 2022.
710

711 Alexander Weiße and Holger Fehske. Exact diagonalization techniques. *Computational many-particle*
712 *physics*, pp. 529–544, 2008.

713 Dian Wu, Lei Wang, and Pan Zhang. Solving statistical mechanics using variational autoregressive
714 networks. *Physical review letters*, 122(8):080602, 2019.
715

716 Tailong Xiao, Jingzheng Huang, Hongjing Li, Jianping Fan, and Guihua Zeng. Intelligent certification
717 for quantum simulators via machine learning. *npj Quantum Information*, 8(1):138, 2022.

718 Zhilin Yang, Zihang Dai, Yiming Yang, Jaime Carbonell, Russ R Salakhutdinov, and Quoc V Le.
719 Xlnet: Generalized autoregressive pretraining for language understanding. *Advances in neural*
720 *information processing systems*, 32, 2019.
721

722 Yuchen Zhu, Tianrong Chen, Evangelos A Theodorou, Xie Chen, and Molei Tao. Quantum state
723 generation with structure-preserving diffusion model. *arXiv preprint arXiv:2404.06336*, 2024.
724
725
726
727
728
729
730
731
732
733
734
735
736
737
738
739
740
741
742
743
744
745
746
747
748
749
750
751
752
753
754
755

A DETAILED DERIVATION OF EQ. 6

To derive the expanded form of the KL divergence in the learning objective, we start from the definition of the KL divergence, which is given as

$$\mathcal{L}_{\text{KL}} = \mathbb{E}_{p(\mathbf{z}_{0:T}|\boldsymbol{\sigma})} \left[\log \frac{p(\mathbf{z}_T|\mathbf{z}_0)}{q(\mathbf{z}_T)} + \sum_{t=2}^T \log \frac{p(\mathbf{z}_{t-1}|\mathbf{z}_t, \mathbf{z}_0)}{q_{\boldsymbol{\theta}}(\mathbf{z}_{t-1}|\mathbf{z}_t)} + \log \frac{\tilde{p}_{\delta}(\mathbf{z}_0|\boldsymbol{\sigma})}{q_{\boldsymbol{\theta}}(\mathbf{z}_0|\mathbf{z}_1)} \right]. \quad (11)$$

Note that the KL divergence between p and q is defined as

$$\mathcal{L}_{\text{KL}} = \mathbb{E}_p \left[\log \frac{p}{q} \right]. \quad (12)$$

Given that p is $p(\mathbf{z}_{0:T}|\boldsymbol{\sigma})$ and q is $q_{\boldsymbol{\theta}}(\mathbf{z}_{0:T}|\mathbf{x})$, the KL divergence should be

$$\mathcal{L}_{\text{KL}} = \mathbb{E}_{p(\mathbf{z}_{0:T}|\boldsymbol{\sigma})} \left[\log \frac{p(\mathbf{z}_{0:T}|\boldsymbol{\sigma})}{q_{\boldsymbol{\theta}}(\mathbf{z}_{0:T}|\mathbf{x})} \right]. \quad (13)$$

Both p and q are Markov chains and can be factorized. The forward process $p(\mathbf{z}_{0:T}|\boldsymbol{\sigma})$ can be factorized as

$$p(\mathbf{z}_{0:T}|\boldsymbol{\sigma}) = \tilde{p}_{\delta}(\mathbf{z}_0|\boldsymbol{\sigma}) \prod_{t=1}^T p(\mathbf{z}_t|\mathbf{z}_{t-1}). \quad (14)$$

And the reverse process $q_{\boldsymbol{\theta}}(\mathbf{z}_{0:T}|\mathbf{x})$ can be also factorized as

$$q_{\boldsymbol{\theta}}(\mathbf{z}_{0:T}|\mathbf{x}) = q(\mathbf{z}_T) \prod_{t=1}^T q_{\boldsymbol{\theta}}(\mathbf{z}_{t-1}|\mathbf{z}_t). \quad (15)$$

Here, $\tilde{p}_{\delta}(\mathbf{z}_0|\boldsymbol{\sigma})$ is the initial distribution, $p(\mathbf{z}_t|\mathbf{z}_{t-1})$ is the forward noising process, and $q_{\boldsymbol{\theta}}(\mathbf{z}_{t-1}|\mathbf{z}_t)$ is the reverse denoising process. Substitute the factorized forms into the KL divergence and we can get

$$\begin{aligned} \mathcal{L}_{\text{KL}} &= \mathbb{E}_{p(\mathbf{z}_{0:T}|\boldsymbol{\sigma})} \left[\log \tilde{p}_{\delta}(\mathbf{z}_0|\boldsymbol{\sigma}) + \sum_{t=1}^T \log p(\mathbf{z}_t|\mathbf{z}_{t-1}) - \left(\log q(\mathbf{z}_T) + \sum_{t=1}^T \log q_{\boldsymbol{\theta}}(\mathbf{z}_{t-1}|\mathbf{z}_t) \right) \right] \\ &= \mathbb{E}_{p(\mathbf{z}_{0:T}|\boldsymbol{\sigma})} \left[(\log \tilde{p}_{\delta}(\mathbf{z}_0|\boldsymbol{\sigma}) - \log q_{\boldsymbol{\theta}}(\mathbf{z}_0|\mathbf{z}_1)) + \sum_{t=1}^{T-1} (\log p(\mathbf{z}_t|\mathbf{z}_{t-1}) - \log q_{\boldsymbol{\theta}}(\mathbf{z}_t|\mathbf{z}_{t+1})) \right. \\ &\quad \left. + \log p(\mathbf{z}_T|\mathbf{z}_{T-1}) - \log q(\mathbf{z}_T) \right]. \end{aligned} \quad (16)$$

We can express $p(\mathbf{z}_t|\mathbf{z}_{t-1})$ in terms of $p(\mathbf{z}_{t-1}|\mathbf{z}_t, \mathbf{z}_0)$ using the properties of the Gaussian distributions in the diffusion process. First, recall that in the forward process, the joint distribution $p(\mathbf{z}_{0:T}|\boldsymbol{\sigma})$ can be rewritten using the posterior distributions $p(\mathbf{z}_{t-1}|\mathbf{z}_t, \mathbf{z}_0)$:

$$p(\mathbf{z}_{0:T}|\boldsymbol{\sigma}) = \tilde{p}_{\delta}(\mathbf{z}_0|\boldsymbol{\sigma}) p(\mathbf{z}_T|\mathbf{z}_0) \prod_{t=2}^T p(\mathbf{z}_{t-1}|\mathbf{z}_t, \mathbf{z}_0). \quad (17)$$

This is possible because the diffusion process allows us to compute $p(\mathbf{z}_{t-1}|\mathbf{z}_t, \mathbf{z}_0)$, which is Gaussian. Then we substitute the new expression into the KL divergence:

$$\mathcal{L}_{\text{KL}} = \mathbb{E}_{p(\mathbf{z}_{0:T}|\boldsymbol{\sigma})} \left[\log \tilde{p}_{\delta}(\mathbf{z}_0|\boldsymbol{\sigma}) - \log q_{\boldsymbol{\theta}}(\mathbf{z}_0|\mathbf{z}_1) + \log p(\mathbf{z}_T|\mathbf{z}_0) - \log q(\mathbf{z}_T) + \sum_{t=2}^T (\log p(\mathbf{z}_{t-1}|\mathbf{z}_t, \mathbf{z}_0) - \log q_{\boldsymbol{\theta}}(\mathbf{z}_{t-1}|\mathbf{z}_t)) \right]. \quad (18)$$

Now, the KL divergence becomes:

$$\mathcal{L}_{\text{KL}} = \mathbb{E}_{p(\mathbf{z}_{0:T}|\boldsymbol{\sigma})} \left[\log \frac{\tilde{p}_{\delta}(\mathbf{z}_0|\boldsymbol{\sigma})}{q_{\boldsymbol{\theta}}(\mathbf{z}_0|\mathbf{z}_1)} + \log \frac{p(\mathbf{z}_T|\mathbf{z}_0)}{q(\mathbf{z}_T)} + \sum_{t=2}^T \log \frac{p(\mathbf{z}_{t-1}|\mathbf{z}_t, \mathbf{z}_0)}{q_{\boldsymbol{\theta}}(\mathbf{z}_{t-1}|\mathbf{z}_t)} \right]. \quad (19)$$

The derivation is completed. We can further interpret each term in the expanded KL divergence as follows.

- Initial KL Term ($t = 0$).

$$\mathbb{E}_{p(\mathbf{z}_0|\boldsymbol{\sigma})} \left[\log \frac{\tilde{p}_\delta(\mathbf{z}_0|\boldsymbol{\sigma})}{q_\theta(\mathbf{z}_0|\mathbf{z}_1)} \right]. \quad (20)$$

This term measures the discrepancy between the initial embedding distribution $\tilde{p}_\delta(\mathbf{z}_0|\boldsymbol{\sigma})$ and the model’s initial reconstruction $q_\theta(\mathbf{z}_0|\mathbf{z}_1)$.

- Final KL Term ($t = T$).

$$\mathbb{E}_{p(\mathbf{z}_T|\mathbf{z}_0)} \left[\log \frac{p(\mathbf{z}_T|\mathbf{z}_0)}{q(\mathbf{z}_T)} \right]. \quad (21)$$

This term compares the noise distribution at time T conditioned on \mathbf{z}_0 with the standard Gaussian prior $q(\mathbf{z}_T)$.

- Intermediate KL Terms ($2 \leq t \leq T$).

$$\sum_{t=2}^T \mathbb{E}_{p(\mathbf{z}_{t-1}, \mathbf{z}_t|\mathbf{z}_0)} \left[\log \frac{p(\mathbf{z}_{t-1}|\mathbf{z}_t, \mathbf{z}_0)}{q_\theta(\mathbf{z}_{t-1}|\mathbf{z}_t)} \right]. \quad (22)$$

These terms measure the discrepancy between the true posterior $p(\mathbf{z}_{t-1}|\mathbf{z}_t, \mathbf{z}_0)$ and the model’s predicted distribution $q_\theta(\mathbf{z}_{t-1}|\mathbf{z}_t)$.

B DETAILED DERIVATION OF EQ. 7

To derive the learning objective of Eq. 7, we first review some notations and definitions of diffusion models and the KL divergence in the main body of the paper as follows.

Measurement String: $\boldsymbol{\sigma} = (\sigma_1, \dots, \sigma_L)$, a sequence of discrete tokens. *Physical Condition:* \mathbf{x} , a sequence of physical variables conditioning the ground state of the Hamiltonian $H(\mathbf{x})$. *Token Embeddings:* $\text{EMB}(\boldsymbol{\sigma}) \in \mathbb{R}^{L \times d}$, continuous embeddings of the measurement string. *Initial Embedding Distribution:* $\tilde{p}_\delta(\mathbf{z}_0|\boldsymbol{\sigma}) = \mathcal{N}(\mathbf{z}_0; \text{EMB}(\boldsymbol{\sigma}), \beta_0 I)$. *Forward Process:* Adds noise to \mathbf{z}_0 to obtain $\mathbf{z}_1, \dots, \mathbf{z}_T$, with transitions $p(\mathbf{z}_t|\mathbf{z}_{t-1}) = \mathcal{N}(\mathbf{z}_t; \sqrt{1 - \beta_t} \mathbf{z}_{t-1}, \beta_t I)$. *Reverse Process:* Starts from $\mathbf{z}_T \sim \mathcal{N}(0, I)$ and predicts \mathbf{z}_0 using $q_\theta(\mathbf{z}_{t-1}|\mathbf{z}_t, \mathbf{x}) = \mathcal{N}(\mathbf{z}_{t-1}; \mu_\theta(\mathbf{z}_t, \mathbf{x}, t), \gamma(t)I)$.

Then we derive this equation. The KL divergence between the forward process $p(\mathbf{z}_{0:T}|\boldsymbol{\sigma})$ and the reverse process $q_\theta(\mathbf{z}_{0:T}|\mathbf{x})$ is

$$\mathcal{L}_{\text{KL}} = \mathbb{E}_{p(\mathbf{z}_{0:T}|\boldsymbol{\sigma})} \left[\log \frac{p(\mathbf{z}_{0:T}|\boldsymbol{\sigma})}{q_\theta(\mathbf{z}_{0:T}|\mathbf{x})} \right]. \quad (23)$$

Expanding the joint distributions and we obtain

$$\begin{aligned} p(\mathbf{z}_{0:T}|\boldsymbol{\sigma}) &= \tilde{p}_\delta(\mathbf{z}_0|\boldsymbol{\sigma}) \prod_{t=1}^T p(\mathbf{z}_t|\mathbf{z}_{t-1}), \\ q_\theta(\mathbf{z}_{0:T}|\mathbf{x}) &= q(\mathbf{z}_T) \prod_{t=1}^T q_\theta(\mathbf{z}_{t-1}|\mathbf{z}_t, \mathbf{x}). \end{aligned} \quad (24)$$

Substituting back into the KL divergence and we obtain

$$\mathcal{L}_{\text{KL}} = \mathbb{E}_{p(\mathbf{z}_{0:T}|\boldsymbol{\sigma})} \left[\log \tilde{p}_\delta(\mathbf{z}_0|\boldsymbol{\sigma}) - \log q_\theta(\mathbf{z}_0|\mathbf{z}_1, \mathbf{x}) + \sum_{t=1}^T (\log p(\mathbf{z}_t|\mathbf{z}_{t-1}) - \log q_\theta(\mathbf{z}_{t-1}|\mathbf{z}_t, \mathbf{x})) - \log q(\mathbf{z}_T) \right]. \quad (25)$$

Then the KL divergence is broken down and we can reorganize the KL divergence into terms corresponding to each timestep. The formulation is given as

$$\mathcal{L}_{\text{KL}} = \mathbb{E}_{p(\mathbf{z}_{0:T}|\boldsymbol{\sigma})} \left[\text{KL}(p(\mathbf{z}_T|\mathbf{z}_0) \| q(\mathbf{z}_T)) + \sum_{t=2}^T \text{KL}(p(\mathbf{z}_{t-1}|\mathbf{z}_t, \mathbf{z}_0) \| q_\theta(\mathbf{z}_{t-1}|\mathbf{z}_t, \mathbf{x})) + \text{KL}(p(\mathbf{z}_0|\mathbf{z}_1, \boldsymbol{\sigma}) \| q_\theta(\mathbf{z}_0|\mathbf{z}_1, \mathbf{x})) \right]. \quad (26)$$

For Gaussian distributions, the KL divergence between $p = \mathcal{N}(\mu_p, \Sigma_p)$ and $q = \mathcal{N}(\mu_q, \Sigma_q)$ is

$$\text{KL}(p \| q) = \frac{1}{2} \left[\text{tr}(\Sigma_q^{-1} \Sigma_p) + (\mu_q - \mu_p)^\top \Sigma_q^{-1} (\mu_q - \mu_p) - k + \ln \left(\frac{\det \Sigma_q}{\det \Sigma_p} \right) \right], \quad (27)$$

where k is the dimensionality. Given that variances are fixed and known, and constants can be ignored during optimization, the KL divergence reduces to

$$\text{KL}(p||q) \propto \|\mu_q - \mu_p\|^2. \quad (28)$$

Now we can specify the KL divergence at each time step. For $t = 1$, the KL divergence between $p(\mathbf{z}_0|\mathbf{z}_1, \boldsymbol{\sigma})$ and $q_\theta(\mathbf{z}_0|\mathbf{z}_1, \mathbf{x})$ is:

$$\text{KL}(p(\mathbf{z}_0|\mathbf{z}_1, \boldsymbol{\sigma})||q_\theta(\mathbf{z}_0|\mathbf{z}_1, \mathbf{x})) \propto \|\mu_\theta(\mathbf{z}_1, \mathbf{x}, 1) - \tilde{\mu}_1(\mathbf{z}_1, \text{EMB}(\boldsymbol{\sigma}))\|^2, \quad (29)$$

where $\tilde{\mu}_1(\mathbf{z}_1, \text{EMB}(\boldsymbol{\sigma}))$ is the true posterior mean from the forward process. When the time step $t \geq 2$, for each t we have

$$\text{KL}(p(\mathbf{z}_{t-1}|\mathbf{z}_t, \mathbf{z}_0)||q_\theta(\mathbf{z}_{t-1}|\mathbf{z}_t, \mathbf{x})) \propto \|\mu_\theta(\mathbf{z}_t, \mathbf{x}, t) - \tilde{\mu}_t(\mathbf{z}_t, \mathbf{z}_0)\|^2. \quad (30)$$

In the forward process, the posterior mean $\tilde{\mu}_t$ is a linear combination of \mathbf{z}_t and \mathbf{z}_0 given by

$$\tilde{\mu}_t(\mathbf{z}_t, \mathbf{z}_0) = \frac{\sqrt{\bar{\alpha}_{t-1}}\beta_t}{1 - \bar{\alpha}_t}\mathbf{z}_0 + \frac{\sqrt{\bar{\alpha}_t}(1 - \bar{\alpha}_{t-1})}{1 - \bar{\alpha}_t}\mathbf{z}_t. \quad (31)$$

When β_t is small, we can approximate $\tilde{\mu}_t(\mathbf{z}_t, \mathbf{z}_0) \approx \mathbf{z}_0$. Substituting the approximations back into the KL divergence terms and we obtain the term for $t = 1$ is

$$\|\mu_\theta(\mathbf{z}_1, \mathbf{x}, 1) - \text{EMB}(\boldsymbol{\sigma})\|^2. \quad (32)$$

The term for $t \leq 2$ is

$$\|\mu_\theta(\mathbf{z}_t, \mathbf{x}, t) - \mathbf{z}_0\|^2. \quad (33)$$

The rounding step involves mapping \mathbf{z}_0 back to the discrete measurements $\boldsymbol{\sigma}$ using $\tilde{q}_\theta(\boldsymbol{\sigma}|\mathbf{z}_0)$. The negative log-likelihood of this step is

$$-\mathbb{E}_{p(\mathbf{z}_0|\mathbf{x}, \mathbf{z}_{1:T})} \log \tilde{q}_\theta(\boldsymbol{\sigma}|\mathbf{z}_0). \quad (34)$$

Then we can combine all terms, the learning objective becomes to minimize

$$\mathcal{L} = \mathbb{E}_{\mathbf{x}, \boldsymbol{\sigma}} \left[\|\text{EMB}(\boldsymbol{\sigma}) - \mu_\theta(\mathbf{z}_1, \mathbf{x}, 1)\|^2 + \sum_{t=2}^T \|\mathbf{z}_0 - \mu_\theta(\mathbf{z}_t, \mathbf{x}, t)\|^2 - \log \tilde{q}_\theta(\boldsymbol{\sigma}|\mathbf{z}_0) \right]. \quad (35)$$

This objective encourages the model to minimize the difference between the predicted means $\mu_\theta(\mathbf{z}_t, \mathbf{x}, t)$ and the true values (EMB($\boldsymbol{\sigma}$) at $t = 1$ and \mathbf{z}_0 for $t \geq 2$), and encourages to maximize the likelihood of reconstructing the measurement string $\boldsymbol{\sigma}$ from \mathbf{z}_0 .

C MORE BASICS OF QUANTUM STATES AND QUANTUM MEASUREMENTS

In this section, we provide more details about the quantum states and quantum measurements and their relationship with classical joint distribution. For a comprehensive discussion, we refer the readers who are interested in quantum computing and quantum information to the Section 2.1 of the book [Nielsen & Chuang \(2010\)](#).

A single qubit – the smallest unit of quantum computing – is mathematically represented as a vector $|\psi\rangle = \alpha|0\rangle + \beta|1\rangle$ parameterized by two complex numbers satisfying $|\alpha|^2 + |\beta|^2 = 1$. Operations on a qubit must preserve this norm, and thus are described by 2×2 unitary matrices. Of these, some of the most important are the Pauli operators; it is useful to list them here:

$$X \equiv \begin{bmatrix} 0 & 1 \\ 1 & 0 \end{bmatrix}, \quad Y \equiv \begin{bmatrix} 0 & -i \\ i & 0 \end{bmatrix}, \quad Z \equiv \begin{bmatrix} 1 & 0 \\ 0 & -1 \end{bmatrix}. \quad (36)$$

One could do some linear algebras and check that $|0\rangle = \begin{bmatrix} 1 \\ 0 \end{bmatrix}$ and $|1\rangle = \begin{bmatrix} 0 \\ 1 \end{bmatrix}$ are the eigenvectors of Z , $|+\rangle = \frac{1}{\sqrt{2}} \begin{bmatrix} 1 \\ 1 \end{bmatrix}$ and $|-\rangle = \frac{1}{\sqrt{2}} \begin{bmatrix} 1 \\ -1 \end{bmatrix}$ are the eigenvectors of X , $|i_+\rangle = \frac{1}{\sqrt{2}} \begin{bmatrix} 1 \\ i \end{bmatrix}$ and $|i_-\rangle = \frac{1}{\sqrt{2}} \begin{bmatrix} 1 \\ -i \end{bmatrix}$ are the eigenvectors of Y . The same qubit can be decomposed in to different orthonormal basis. For example,

$$\begin{aligned} |\psi\rangle &= \alpha|0\rangle + \beta|1\rangle \\ &= \frac{1}{\sqrt{2}}(\alpha + \beta)|+\rangle + \frac{1}{\sqrt{2}}(\alpha - \beta)|-\rangle \\ &= \frac{1}{\sqrt{2}}(\alpha - \beta i)|i_+\rangle + \frac{1}{\sqrt{2}}(\alpha + \beta i)|i_-\rangle. \end{aligned} \quad (37)$$

Positive-operator valued measurement (POVM) is the testing or manipulation of a physical system to yield a numerical result. POVM is described by a set of measurement operators $\{\Pi_k\}_{k=0}^{K-1}$ satisfying $\sum_k \Pi_k = \mathbf{I}$ and each Π_k is positive semi-definite, where K is the total number of measurement operators. In this paper, we consider the Pauli-6 POVM (also named as randomized single-qubit Pauli measurements in some literature) such that the measurement operators are $\{\frac{1}{3}|0\rangle\langle 0|, \frac{1}{3}|1\rangle\langle 1|, \frac{1}{3}|+\rangle\langle +|, \frac{1}{3}|-\rangle\langle -|, \frac{1}{3}|i_+\rangle\langle i_+|, \frac{1}{3}|i_-\rangle\langle i_-\rangle\}$. It is easy to check that these operators satisfy the POVM definition and $K = 6$. The reason for choosing the Pauli-6 POVM is that this measurement protocol is easy to be implemented on current quantum devices (NISQ devices) and is informative-completed (IC).

Measuring a qubit leads to collapse of the qubit and produces an outcome k with the probability $p(k)$ satisfying the Born rule, which states that $p(k) = \text{tr}(\rho \Pi_k)$, where $\rho = |\psi\rangle\langle\psi|$ and $\langle\psi|$ is the transpose conjugate of $|\psi\rangle$. We may consider a system of L qubits. It can be described by the wave function:

$$|\Phi\rangle = \sum_{\sigma_1=1}^M \cdots \sum_{\sigma_L=1}^M \Psi(\sigma_1, \dots, \sigma_L) |\sigma_1, \dots, \sigma_L\rangle,$$

where $\Psi : \mathbb{Z}^L \rightarrow \mathbb{C}$ maps a fixed configuration $\sigma = (\sigma_1, \dots, \sigma_L)$ of L qubits to a complex number which is the amplitude satisfying $\sum_{\sigma_1=1}^K \cdots \sum_{\sigma_L=1}^K |\Psi(\sigma_1, \dots, \sigma_L)|^2 = 1$, and $\sigma_i \in \{1, \dots, K\}$ is one of the K possible outcomes by performing quantum measurement on the i -th qubit. It is formulated in a complex Hilbert space where the vector representation of the quantum state $|\Phi\rangle \in \mathbb{C}^{K^L}$ and its density matrix $|\Phi\rangle\langle\Phi| \in \mathbb{C}^{K^L \times K^L}$, which becomes astronomical for large L .

Performing quantum measurement independently on L qubits is easy to be implemented. The most common strategy is to combine L single-qubit measurement operators to $\Pi_{k,1} \otimes \cdots \otimes \Pi_{k,L}$ where \otimes is the Kronecker product. Such measurement procedure outputs a measurement string $\sigma = (\sigma_1, \dots, \sigma_L)$ where $\sigma_i \in \{1, \dots, K\}$ with probability $|\Psi(\sigma_1, \dots, \sigma_L)|^2$. Define $p(\sigma_1, \dots, \sigma_L) = |\Psi(\sigma_1, \dots, \sigma_L)|^2$. We can reformulate the wave function of quantum states to a classical joint distribution. It is a valid and legal joint distribution since $\sum_{\sigma_1} \cdots \sum_{\sigma_L} p(\sigma_1, \dots, \sigma_L) = \sum_{\sigma_1} \cdots \sum_{\sigma_L} |\Psi(\sigma_1, \dots, \sigma_L)|^2 = 1$ and $p(\sigma_1, \dots, \sigma_L) \geq 0$.

D DETAILS FOR BASELINE MODELS

We consider the classical shadow (CS) method (Huang et al., 2020), a state-of-the-art, learning-free approach for efficiently constructing representations of unknown quantum states. For learning-based comparisons, we include kernel methods such as the Radial Basis Function Kernel (RBFK) and Neural Tangent Kernel (NTK) following the implementation in Huang et al. (2022). Additionally, we evaluate advanced neural network-based models, including a Recurrent Neural Network (RNN)-based architecture (Carrasquilla et al., 2019) and the transformer-based state-of-the-art model LLM4QPE (Tang et al., 2024). The details about their configurations are as follows.

Classical Shadow (Huang et al., 2020). Classical Shadow (CS) is a learning-free protocol used to efficiently predict many properties of quantum states with a logarithmic number of measurements. By using randomized measurements and building a memory-efficient representation of the quantum state, it enables the estimation of various properties with high accuracy.

Kernel Methods (Huang et al., 2022). We utilize Radial Basis Function Kernel (RBFK) and Neural Tangent Kernel (NTK) to learn the feature map from physical conditions \mathbf{x} to certain properties of the ground state of the Hamiltonian $H(\mathbf{x})$. A grid search is performed to identify the optimal regularization strength, with candidate values uniformly distributed on a logarithmic scale from 0.001 to 100. We employ a 5-fold cross-validation strategy on the training dataset and present the predictive performance of the model that achieves the highest accuracy on the test dataset.

RNN (Carrasquilla et al., 2019). Recurrent Neural Networks (RNNs) are employed to reconstruct quantum states from measurement data, leveraging their ability to capture temporal or sequential dependencies. In our implementation, the RNN takes a sequence of measurement outcomes as input and learns to predict the underlying quantum state properties by modeling correlations between successive measurements. The model architecture includes a hidden layer with 128 units and is trained using the Adam optimizer. To ensure fair comparison, we perform early stopping based on validation loss and use the test dataset for final evaluation of predictive performance.

Table 3: RMSE of predicting the correlations of all subsystems of size two on the test dataset. The result is averaged over Heisenberg model instances and each pair of adjacent qubits. For CS, M denotes the number of input measurements. While for the neural network-based approaches M denotes the number of sampled measurements M_{out} from trained models. The standard deviations are distinguished in gray.

Method	$L = 10$				$L = 40$				$L = 70$				$L = 100$			
	$M = 100$	1000	10000	20000	100	1000	10000	20000	100	1000	10000	20000	100	1000	10000	20000
CS	0.1564	0.0509	0.0156	0.0107	0.1696	0.0538	0.0173	0.0121	0.1771	0.0545	0.0172	0.0121	0.1724	0.0547	0.0172	0.0122
RBFK		0.0796				0.0639				0.0578				0.0493		
NTK		0.0775				0.0622				0.0565				0.0470		
RNN	0.1328	0.0502	0.0145	0.0119	0.1795	0.0671	0.0164	0.0118	0.2137	0.0739	0.0240	0.0153	0.2325	0.0806	0.0251	0.0163
	0.0342	0.0098	0.0024	0.0014	0.0388	0.0132	0.0035	0.0016	0.0453	0.0149	0.0037	0.0025	0.0419	0.0094	0.0043	0.0039
LLM4QPE	0.1316	0.0489	0.0136	0.0093	0.1624	0.0513	0.0142	0.0097	0.1814	0.0527	0.0155	0.0116	0.1759	0.0531	0.0152	0.0114
	0.0379	0.0140	0.0032	0.0015	0.0392	0.0128	0.0032	0.0017	0.0462	0.0157	0.0038	0.0021	0.0493	0.0082	0.0056	0.0028
Ours	0.1269	0.0432	0.0097	0.0085	0.1582	0.0465	0.0113	0.0091	0.1679	0.0473	0.0117	0.0092	0.1686	0.0478	0.0125	0.0098
	0.0365	0.0097	0.0022	0.0008	0.0416	0.0115	0.0037	0.0004	0.0479	0.0138	0.0029	0.0011	0.0512	0.0083	0.0036	0.0009

Table 4: RMSE of predicting the entanglement entropies of all subsystems of size two on the test dataset. The result is averaged over Heisenberg model instances and each pair of adjacent qubits. For CS, M denotes the number of input measurements. While for the neural network-based approaches M denotes the number of sampled measurements M_{out} from trained models. The standard deviations are distinguished in gray.

Method	$L = 10$				$L = 40$				$L = 70$				$L = 100$			
	$M = 100$	1000	10000	20000	100	1000	10000	20000	100	1000	10000	20000	100	1000	10000	20000
CS	0.5966	0.0922	0.0204	0.0119	0.6487	0.0927	0.0294	0.0259	0.6421	0.0943	0.0312	0.0298	0.6518	0.0998	0.0357	0.0316
RBFK		0.1268				0.1037				0.0997				0.0752		
NTK		0.1379				0.1034				0.0983				0.0719		
RNN	0.5225	0.1164	0.0187	0.0115	0.6132	0.1054	0.0246	0.0212	0.7948	0.1305	0.0514	0.0385	0.8229	0.1476	0.0617	0.0439
	0.0833	0.0263	0.0022	0.0014	0.0945	0.0314	0.0026	0.0015	0.0997	0.0302	0.0048	0.0026	0.0957	0.0269	0.0054	0.0032
LLM4QPE	0.4937	0.0948	0.0176	0.0102	0.5878	0.0896	0.0223	0.0207	0.6258	0.0912	0.0276	0.0251	0.6392	0.1055	0.0312	0.0286
	0.0932	0.0168	0.0023	0.0012	0.0845	0.0209	0.0016	0.0011	0.0940	0.0235	0.0016	0.0018	0.0979	0.0212	0.0020	0.0018
Ours	0.5479	0.0867	0.0132	0.0089	0.5629	0.0861	0.0187	0.0145	0.5970	0.0879	0.0245	0.0218	0.6125	0.0928	0.0281	0.0243
	0.0952	0.0079	0.0019	0.0011	0.0822	0.0196	0.0021	0.0009	0.0835	0.0194	0.0014	0.0012	0.0857	0.0163	0.0018	0.0014

LLM4QPE (Tang et al., 2024). It presents a transformer-based approach for predicting various properties of quantum systems through a pre-training procedure that maximizes a likelihood function based on discrete measurement outcomes. This is also a generative process similar to the conditional quantum state modeling discussed in Wang et al. (2022). The trained model can generate measurement samples conditioned on the physical parameters which are unseen from the training dataset. Afterwards the quantum properties can be analyzed by using post-processing such as classical shadow. For a fair comparison, we set the model with 4 heads, 4 layers, and a hidden dimension of 128.

RydbergGPT (Fitzek et al., 2024). It utilizes autoregressive transformers, employs KL divergence as the loss function, and learns from large quantum measurement datasets to approximate the classical joint distribution of the quantum state. Predictions of specific quantum properties are then made by sampling from this learned distribution. For a fair comparison, we set the model with 4 heads, 4 layers, and a hidden dimension of 128. We also add a linear projection layer at the transformer’s output (K output units with softmax).

E VISUALIZED SUPPLEMENT OF THE COMPARISON BETWEEN QUADIM AND AUTOREGRESSIVE BASELINE

We include an additional plot in Fig. 6, where we present a more fine-grained visualization of the prediction performance of QuaDiM. In this figure, each point represents the absolute error between the predicted correlation and the ground truth for all pairs of qubits across different M_{out} .

1026
1027
1028
1029
1030
1031
1032
1033
1034
1035
1036
1037
1038
1039
1040
1041
1042
1043
1044
1045
1046
1047
1048
1049
1050
1051
1052
1053
1054
1055
1056
1057
1058
1059
1060
1061
1062
1063
1064
1065
1066
1067
1068
1069
1070
1071
1072
1073
1074
1075
1076
1077
1078
1079

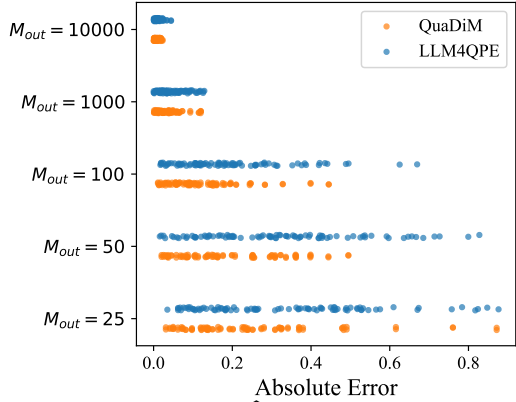


Figure 6: Visualization of predicted correlations \hat{C}_{ij} for the ground state of the 1D anti-ferromagnetic Heisenberg model of length $L = 10$ with different number of samples M_{out} from the trained models. We fix $M_{in} = 1000$ and use classical shadow for post-processing. Each point represents the absolute error (lower is better) between the predicted correlation and the ground truth for all pairs of qubits across different M_{out} .

F ADDITIONAL EXPERIMENT RESULTS

F.1 IMPACT OF DIFFERENT PRE-DEFINED ORDER

To further compare the our model and the autoregressive baselines, we define an alternative ordering of qubits (from right to left or from the largest to the smallest index, as opposed to the left-to-right ordering used throughout the paper) and re-train the autoregressive baselines. The results of RMSE for predicting the correlations of all subsystems of size two on the test dataset, evaluated in the predefined order from right to left, are presented in Tab. 5. For comparison, we also include experimental results already reported in the main text of the paper.

Table 5: RMSE of predicting the correlations of all subsystems of size two on the test dataset under different sequential order. M denotes the number of sampled measurements M_{out} from trained models. Notation \leftarrow denotes from right to left and \rightarrow denotes from left to right.

Method	$L = 70$				$L = 100$			
	$M = 100$	$M = 1000$	$M = 10000$	$M = 20000$	$M = 100$	$M = 1000$	$M = 10000$	$M = 20000$
RNN(\leftarrow)	0.2197	0.0721	0.0216	0.0165	0.2276	0.0763	0.0264	0.0159
RNN(\rightarrow)	0.2137	0.0739	0.0240	0.0153	0.2325	0.0806	0.0251	0.0163
LLM4QPE(\leftarrow)	0.1865	0.0538	0.0157	0.0108	0.1773	0.0542	0.0149	0.0122
LLM4QPE(\rightarrow)	0.1814	0.0527	0.0155	0.0116	0.1759	0.0531	0.0152	0.0114
QuaDiM	0.1679	0.0473	0.0117	0.0092	0.1686	0.0478	0.0125	0.0098

F.2 NUMERICAL RESULTS OF LEARNING LONG-RANGE XY MODEL

To further generalize the effectiveness of our proposed model, we have supplemented our experiments with results from a more physically general and classically challenging system: the long-range XY model in the presence of a transverse field, whose Hamiltonian is given by

$$H_{XY} = \sum_{i < j} J_{ij} (X_i X_j + Y_i Y_j) + \sum_j Z_j \tag{38}$$

where $J_{ij} = J_0/|i - j|^a$ with $a \in (1, 2)$. This quantum model inherits the long-range interactions between every two quantum sites, leading to a complex dynamics which is hard to be simulated by classical computers. We restrict the system size $L = 10$ due to memory limitations. The ground states of quantum systems with different physical conditions J_{ij} are calculated by eigenvalue decomposition. Follow Xiao et al. (2022), we random sample a series of J_{ij} and conduct classical simulations to collect the data. The experimental results for $L = 10$, with $M_{in} = 1000$ and $M_{out} \in \{1000, 10000\}$, are presented in Tab. 6. It can be observed that QuaDiM consistently outperforms baselines.

1080
1081
1082
1083
1084
1085
1086
1087
1088
1089
1090
1091
1092
1093
1094
1095
1096
1097
1098
1099
1100
1101
1102
1103
1104
1105
1106
1107
1108
1109
1110
1111
1112
1113
1114
1115
1116
1117
1118
1119
1120
1121
1122
1123
1124
1125
1126
1127
1128
1129
1130
1131
1132
1133

Table 6: RMSE of predicting the correlations of ground states of the long-range XY model.

Method	$M = 1000$	$M = 10000$
CS	0.2575	0.0517
RBFK		0.1158
NTK		0.1039
RNN	0.2234	0.0502
LLM4QPE	0.2139	0.0482
QuaDiM	0.1986	0.0367

F.3 RESULTS OF VALIDATION ON OUT-OF-DISTRIBUTION DATASET

Here, we consider evaluating the QuaDiM with out-of-distribution (OOD) dataset, which means the dataset used for training and the dataset used for validation come from different distributions. We divide the sampled physical parameters \mathbf{x} into two segments: the training set is limited to $[0, 1.5]$, while the test set exclusively spans $[1.5, 2]$. In alignment with setting of the paper, we set $N^{tr} = 100$ and $N^{te} = 20$. We report the RMSE of predicted correlations for both the sota baseline LLM4QPE, and our model QuaDiM under both OOD and non-OOD (both training and fine-tuning are sampled from the same distribution $[0, 2]$) conditions, with $M_{in} = 1000$ and $M_{out} = 10000$. The results are presented in the Tab. 7.

Table 7: RMSE of predicting the correlations of all subsystems of size two on the test dataset under the out-of-distribution (OOD) condition.

Method	$L = 70$		$L = 100$	
	no OOD	OOD	no OOD	OOD
LLM4QPE	0.0155	0.0526	0.0152	0.0598
QuaDiM	0.0117	0.0417	0.0125	0.0465

F.4 COMPARISON WITH ADDITIONAL BASELINE

We involve RydbergGPT (Fitzek et al., 2024) as a new baseline. It utilizes autoregressive transformers, employs KL divergence as the loss function, and learns from large quantum measurement datasets to approximate the classical joint distribution of the quantum state. Predictions of specific quantum properties are then made by sampling from this learned distribution. For a fair comparison, we set the model with 4 heads, 4 layers, and a hidden dimension of 128. We also add a linear projection layer at the transformer’s output (K output units with `softmax`). we report the RMSE of predicted correlations for $L = 100$ and $M_{in} = 1000$ in Tab. 8.

Table 8: RMSE of predicting the correlations of all subsystems of size two on the test dataset for $L = 100$.

Method	$M = 100$	1000	10000	20000
CS	0.1724	0.0547	0.0172	0.0122
RBFK		0.0493		
NTK		0.0470		
RNN	0.2325	0.0806	0.0251	0.0163
LLM4QPE	0.1759	0.0531	0.0152	0.0114
RydbergGPT	0.1843	0.0562	0.0170	0.0121
Ours	0.1686	0.0478	0.0125	0.0098

F.5 MODEL SENSITIVITY TO THE DENOISING STEPS AND HIDDEN DIMENSION

In this section, we study the relationship between the hyper-parameters including the number of denoising steps T_f and the hidden dimension of QuaDiM and the prediction performance. We fix the number of diffusion steps during training for QuaDiM while shrinking the inference steps T_f using the approach introduced in DDIM (Song et al., 2020). We evaluate the model’s performance under different inference step settings and compare it with both a learning-free baseline (classical shadow, CS) and a learning-based SOTA model LLM4QPE. Due to time constraints, we only report results for the task of predicting correlations with $L = 100$, $M_{in} = 1000$, and $M_{out} = 1000$.

As shown in the Tab. 9, when reducing inference to $T_f = 500$ diffusion steps on a single GPU (2080Ti), QuaDiM achieves a lower RMSE score compared to the classical shadow baseline while demonstrating an inference speed comparable to LLM4QPE.

To further investigate, we evaluate the model’s performance on the task of predicting correlations under a fixed dataset configuration $L = 10$, $M_{in} = 1000$, $M_{out} = 1000$ with different d values from $\{64, 128, 256, 512\}$, and the resulting RMSE scores (lower is better) are: 0.0518, 0.0432, 0.0449, 0.0457, respectively. As the results show, setting $d = 128$ achieves the best performance.

Table 9: RMSE of predicting correlations and the sampling speed with $L = 100$, $M_{in} = 1000$, and $M_{out} = 1000$ under different denoising steps T_f .

Method	RMSE	Generated samples per sec.
CS	0.0547	-
LLM4QPE	0.0531	14.6
QuaDiM ($T_f = 2000$)	0.0478	5.7
QuaDiM ($T_f = 1000$)	0.0537	8.1
QuaDiM ($T_f = 500$)	0.0541	12.7
QuaDiM ($T_f = 100$)	0.0882	37.4

F.6 MODEL SENSITIVITY TO THE POSITIONAL EMBEDDINGS

Positional embeddings in our context are employed to capture the structural information among qubits. Additionally, we further investigate the model’s predicted RMSE in predicting correlations when using relative positional encoding (following the implementation in Shaw et al. (2018)) and no positional encoding at all. Due to time constraints, we only report results for $L = 100$, $M_{in} = 1000$. The experimental results are provided in Tab. 10. Experimental results show that absolute and relative positional embeddings yield comparable performance, but removing positional information altogether significantly degrades the model’s ability to predict quantum correlations. This underscores the embeddings’ role in preserving spatial relationships among qubits.

Table 10: QuaDiM’s RMSE of predicting correlations using different positional embedding (PE) techniques.

	Absolute PE	Relative PE	No PE
$M_{out} = 100$	0.1686	0.1681	0.4527
$M_{out} = 1000$	0.0478	0.0482	0.3269
$M_{out} = 10000$	0.0125	0.0139	0.2895
$M_{out} = 20000$	0.0098	0.0110	0.2148

We acknowledge that the current positional encoding method may not perfectly reflect quantum system-specific structures. As a step forward, we plan to explore customized positional encoding tailored to quantum systems in future work.

F.7 EXPERIMENTS ON TETRAHEDRAL POVM

In the main text of the paper, Pauli-6 POVM is used for data collection because this measurement protocol is easy to implement on current quantum devices (NISQ devices) and is informationally complete (IC). This means that all the information of the quantum state can be recovered classically with a sufficiently large number of IC-POVM measurements. In other words, given the probability of each measurement outcome of IC-POVM, the quantum state can be uniquely determined.

To further validate our method, here we consider another type of IC-POVM: the tetrahedral POVM, to collect measurement data. The corresponding measurement operators are $\{\frac{1}{4}(\mathbf{I} + \mathbf{s}^{(a)} \cdot \mathbf{P})\}_{a \in \{0,1,2,3\}}$, where \mathbf{I} is the identity matrix, \mathbf{P} represents the ensemble of Pauli operators (X, Y, Z) and $\mathbf{s}^{(0)} = (0, 0, 1)$, $\mathbf{s}^{(1)} = (\frac{2\sqrt{2}}{3}, 0, -\frac{1}{3})$, $\mathbf{s}^{(2)} = (-\frac{\sqrt{2}}{3}, \sqrt{\frac{2}{3}}, -\frac{1}{3})$, $\mathbf{s}^{(3)} = (-\frac{\sqrt{2}}{3}, -\sqrt{\frac{2}{3}}, -\frac{1}{3})$. It is easy to check that $K = 4$ for the tetrahedral POVM. Due to time constraints, we fixed $L = 10$ with $M_{in} = 1000$, re-run the simulations to collect data, and re-train our model and the baselines. The numerical results are reported in Tab. 11. As shown, QuaDiM still outperforms the baselines in this scenario.

Table 11: RMSE of predicting correlations using tetrahedral POVM.

Method	M=1000	M=10000
CS	0.0512	0.0164
RBFK		0.0735
NTK		0.0747
RNN	0.0514	0.0163
LLM4QPE	0.0503	0.0141
QuaDiM	0.0433	0.0107

G DISTINCTION FROM THE STUDY IN ZHU ET AL. (2024)

The impracticality of using full density matrix as input in Zhu et al. (2024). One of the principal features distinguishing classical systems from quantum many-body systems is that quantum systems require exponentially many parameters in the system size to fully specify the state (Cramer et al., 2010).

To obtain information from a real quantum system, measurement is required (such as the Pauli measurement used in our paper). Measurement results in discrete outcomes due to the collapse of quantum states. Reconstructing the full density matrix typically demands an exponentially large number of quantum measurements on an actual quantum computer, followed by extensive post-processing of these outcomes, which generally entails exponential overhead (Cramer et al., 2010). As a result, in Zhu et al. (2024) each sample in the training set (i.e., a full density matrix representing a specific quantum state) would require exponential storage space and computational resources, making this approach impractical for real-world applications.

The orthogonality of our task (quantum state property estimation, QPE) to quantum state tomography (QST). The task in Zhu et al. (2024) is more aligned with QST, which seeks to reconstruct the full density matrix. Neural network-based QST (Torlai et al., 2018) generally approximates the probability distribution over the outcomes of an informationally complete measurement using a variational manifold represented by a neural network. However, Zhu et al. (2024) bypasses measurement data entirely and directly uses the density matrix as input. To the best of our knowledge, this approach is impractical, as it contradicts the fundamental constraints of data acquisition, i.e., quantum measurement in quantum systems.

Our focus on QPE. Unlike QST, QPE specifically targets the prediction of specific properties of quantum states without reconstructing the full density matrix. This task has recently garnered significant attention in the quantum physics and machine learning communities, with several cutting-edge theoretical (Huang et al., 2022; Lewis et al., 2023) and empirical (Chen et al., 2023; Tang et al., 2024) studies already published. In terms of model design, unlike the approach of directly modeling the density matrix using generative models, our work delves into bridging the gap between quantum states and the classical joint distributions modeled by generative models. Additionally, we explore how the continuous latent variables of diffusion models can be decoded into discrete quantum measurement data while preserving physical validity.